

Technische Universität München  
Physik Department  
Lehrstuhl für Biophysik, E22

# Active microrheology of semiflexible polymer solutions: computer simulations and scaling theory

Nikita Ter-Oganessian

Vollständiger Abdruck der von der Fakultät für Physik der  
Technischen Universität München  
zur Erlangung des akademischen Grades eines  
Doktors der Naturwissenschaften  
genehmigten Dissertation.

Vorsitzender: Univ.-Prof. Dr. J. Friedrich

Prüfer der Dissertation: 1. Univ.-Prof. Dr. J. L. van Hemmen  
2. Univ.-Prof. Dr. E. Sackmann, em.

Die Dissertation wurde am 23. August 2004 bei der Technischen Universität München eingereicht und durch die Fakultät für Physik am 20. Dezember 2004 angenommen.

# Contents

<b>Abstract</b>	<b>5</b>
<b>1 Microrheology</b>	<b>7</b>
1.1 Experimental techniques . . . . .	7
1.2 Theoretical approach describing rheological measurements . . . . .	9
1.3 Solutions of semiflexible polymers . . . . .	10
1.3.1 High frequency viscoelasticity . . . . .	12
1.3.2 Elastic plateau . . . . .	14
1.3.3 Recent active microrheological experiments on actin solutions . . . . .	16
<b>2 DPD simulation</b>	<b>19</b>
2.1 The dissipative particle dynamics method . . . . .	20
2.2 Constituent equations . . . . .	21
2.3 Polymer model . . . . .	22
2.4 Simulation box and boundary conditions . . . . .	23
2.5 Active microrheology . . . . .	25
2.5.1 Enforced movement of the bead in pure water . . . . .	28
2.5.2 Responses of the bead on external forces . . . . .	30
2.5.3 Distribution of polymers around the moving bead . . . . .	33
2.5.4 Forces resisting the moving bead . . . . .	37
2.5.5 Microrheology of solutions with various concentrations of polymers . . . . .	39
2.5.6 Responses of the bead to various force amplitudes . . . . .	41
2.5.7 Beads of different sizes . . . . .	46
2.5.8 Microrheology of solutions of polymers possessing various diffusion coefficients . . . . .	46
2.6 Conclusions . . . . .	47
<b>3 Diffusion of polymers in solutions</b>	<b>49</b>
3.1 Short time diffusion of semiflexible polymers . . . . .	51

3.2	Long time diffusion of semiflexible polymers . . . . .	55
3.3	Controlling the diffusion coefficient of polymers . . . . .	58
<b>4</b>	<b>Motion of polymers in front of the bead</b>	<b>61</b>
<b>5</b>	<b>Compliance and relaxation modulus in <math>t</math> and <math>\omega</math> domains</b>	<b>65</b>
<b>6</b>	<b>Osmotic force</b>	<b>71</b>
6.1	Osmotic pressure of polymers . . . . .	71
6.2	Osmotic resistance force . . . . .	73
6.3	Motion of the bead . . . . .	73
6.3.1	Square root regime . . . . .	74
6.3.2	Steady state regime . . . . .	75
6.3.3	Characteristic time of the square root regime . . . . .	75
6.4	Comparison with the experiments . . . . .	76
6.5	Comparison with the computer simulations . . . . .	76
<b>7</b>	<b>Steady state regime: asymptotic analytical solution</b>	<b>79</b>
<b>8</b>	<b>Conclusions</b>	<b>83</b>

# Abstract

The present work is motivated by recent experiments on active microrheology of actin solutions. In these experiments response of microbeads in actin solutions to constant forces has been studied and a new regime has been found, in which the bead displacement scales with the square root of time.

In this work we report computer simulations of the enforced bead motion through entangled network of semiflexible polymers modelling the experiments described above.

In the Ch. 2 a simulation model is built on the basis of the Dissipative Particle Dynamics (DPD) method, which is a sort of molecular dynamics method.

The simulations reveal that the response of the bead possesses two regimes. In the initial regime the displacement of the bead is found to be  $y \sim t^{0.75}$ . This regime is followed by  $y = At^\alpha$  with  $\alpha$  taking the values close to 0.5. It is found that this regime lasts for at least two decades in time.

Responses of the bead on various force amplitudes  $f$  are studied and it is found that in the square root regime  $A \sim f$ . The amplitude of the square root regime is shown to depend on the concentration  $c$  of polymers as  $A \sim c^\beta$ , with  $\beta \approx -1.4$ . Simulations of beads of various radii  $R$  show that  $A \sim R^{-1.6}$ .

The simulations reveal that the square root regime is characterized by an increased concentration of polymers in front of the moving bead and a strongly decreased behind with respect to the bulk value. Furthermore, it is found that in the square root regime the force resisting the bead motion is mainly due to polymers and that it is osmotic in origin.

In order to characterize the motion of polymers in active microrheological experiments a study of diffusion of semiflexible polymers in solution is first performed in the Ch. 3. In accordance with the reptation theory it is found that the transversal motion of the polymers is hindered and that they move by means of longitudinal diffusion (reptation). The longitudinal diffusion coefficient  $D_{||}$  of semiflexible polymers is found to be inversely proportional to the contour length of the polymers. No apparent dependence of  $D_{||}$  on the mesh size of the polymer network is observed.

In the Ch. 4 the motion of polymers in front of the moving bead in active microrheological experiments is analyzed. It is found that the polymers in front of the moving bead move by means of longitudinal diffusion with the diffusion coefficient being close to that in the bulk.

Furthermore, it is found that in the square root regime of active microrheology  $A \sim \sqrt{D_{\parallel}}$ .

The Ch. 5 is concerned with interpreting the active microrheological measurements in terms of the complex relaxation modulus  $G^*(\omega)$ . It is shown that the square root regime of the compliance found in the experiments described above as well as in our simulations corresponds to the  $\omega^{0.5}$  scaling of the relaxation modulus with frequency.

On the basis of the performed computer simulations a scaling theory of the active microrheology is suggested in the Ch. 6. The model accounts for the osmotic pressure of polymers due to the suppression of their undulations. The motion of polymers is assumed to be described by the diffusion equation with the diffusion coefficient being that of the longitudinal diffusion. In this framework scaling laws are found for the square root regime as well as for the subsequent viscous-like steady state motion. The results are in good agreement with the experiments as well as with the computer simulations.

Finally, in the Ch. 7 an analytical treatment of the steady state regime of the bead motion is performed. For low external forces the velocity of the bead as well as the concentration distribution of polymers around it are obtained.

# Chapter 1

## Microrheology

### 1.1 Experimental techniques

Microrheology is a rapidly growing field comprising a variety of techniques for measuring local viscoelastic parameters on the scales of microns. There are different motivations for the development of such methods. One of the strongest motivations is that many samples are available only in small quantities. Related to it is the intention to study inhomogeneities in various systems, for example inside living cells. Many systems show different physical properties on different length scales, therefore such techniques provide an ability of probing a particular scale. Furthermore, microrheology techniques extend the capabilities of the conventional macroscopic rheology making possible studies of the viscoelasticity at higher frequencies.

The main principle behind microrheology is that a small spherical probe of micrometer size is introduced into the medium under study and its movement is detected using various techniques. Modern experimental techniques provide spatial resolution up to nanometers. All microrheology methods may be divided into two classes: those employing *active* manipulation of probe particles in the sample, and those utilizing *passive* observation of thermal fluctuations of such probe particles [1, 2]. Both approaches are being developed and improved, they have their advantages and complement each other.

Observation of thermal fluctuations of probes embedded in the studied medium provides information about its rheological properties. This is because the thermal fluctuations reflect the linear response parameters of the medium and their complete frequency dependence. Thermal fluctuations of a single or several probes can be observed and analyzed, as well as a simultaneous averaging over the whole ensemble of the embedded particles can be done using light scattering methods.

One of such methods is the diffusing wave spectroscopy (DWS) [3]. The intensity of the multiply scattered light fluctuates over time due to the relative motion of individual scattering elements and is sensitive to their displacements much smaller than the wavelength of light. Moreover, an extraordinarily wide range of timescales can be probed, from  $10^{-8}$  to  $10^5$  s. The DWS technique has been used to study the properties of various systems, including colloids, polymer solutions and gels [4].

The basic advantage of the DWS technique over various single-particle tracking methods is that an ensemble average over many particles is intrinsically performed. In contrast, in the single-particle tracking it may be necessary to average the results for many different particles in order to obtain a statistically meaningful measurement. On the other hand, observation of the motion of single particles permits the study of inhomogeneities within the sample.

The spatial resolution of various microscopical methods reaches nanometer scale favoring their extensive use in the microrheological studies. Increasing temporal resolution provides a wide frequency range permitting measuring of particle displacements over short times. The measured mean square displacement of the thermally fluctuating particle allows the determination of local viscoelastic parameters of the embedding medium [1]. Methods based on cross correlating the thermal motion of pairs of embedded probe particles, the so-called two-point microrheology, are believed to determine the viscoelastic behavior of soft materials more accurately than do the conventional single-particle methods [5, 6].

The *active* manipulation of micron-size particles dates back to the early 1920s when the properties of gelatin were studied using small magnetic particles [7]. Recent advances in high-resolution and rapid microscopy have led to increased interest in similar micromanipulation techniques, magnetic tweezers. This method is based on the fact that inhomogeneous magnetic field exerts a force on the magnetic particle embedded in the studied sample. Local viscoelastic responses of biopolymer solutions and gels have been studied using magnetic tweezers [8–11], as well as the viscoelastic properties of cell membranes and cell compartments [12, 13].

The applied forces in such techniques are calibrated by measuring the velocity of the same kind of bead exposed to the same field gradient in a purely viscous fluid of known viscosity. The values of the forces exerted on the magnetic beads cover the range from  $\sim 1$  pN to tens of  $\sim 10$  nN. The length of the applied force pulses has some limitations due to the overheating of the magnetic coil but can be extended currently up to several minutes.

Other methods of active microrheology include optical tweezers, which is similar to the magnetic tweezers method except that the force is exerted on

the probe particle with the help of an optical laser trap [14], and methods based on the atomic force microscopy.

In the family of the active microrheological methods described above, there exist methods concerned with the determination of the strain field around the probe particle, employing, for example, non-magnetic beads, which are embedded in the vicinity of the magnetic probe. The deformation of the surroundings of the probe particle caused by its displacement when the external force is applied can be mapped by observing the respective displacements of the non-magnetic beads [10].

## 1.2 Theoretical approach describing rheological measurements

Fundamental to any kind of rheology using probe particles is a quantitative modelling of the interaction of the probe with its surroundings. One of the key characteristics describing the linear viscoelastic behavior of a complex fluid is the relaxation modulus  $G(t)$ . The relaxation modulus relates the time dependent strain in the system  $\gamma(t)$  to the stress  $\sigma(t)$

$$\sigma(t) = \int_{-\infty}^t G(t-t') \dot{\gamma}(t') dt', \quad (1.1)$$

where the dot indicates the time derivative. The Laplace transform of the relaxation modulus is extensively used

$$G^*(\omega) = i\omega \int_0^{\infty} G(t) e^{-i\omega t} dt, \quad (1.2)$$

revealing the response of the medium to an oscillating stress  $\sigma(\omega) = G^*(\omega) \gamma(\omega)$ . The real  $G'(\omega)$  and imaginary  $G''(\omega)$  parts of the complex relaxation modulus  $G^*(\omega)$  are called storage and loss modulus, respectively. These quantities, as the names suggest, reflect respectively the elastic and the dissipative components of the complex viscoelastic behavior. It is useful to mention that the storage and loss moduli are not independent in fact. As a consequence of the causality principle these quantities are interrelated through the Kramers-Kronig relations [15].

Instead of the relaxation modulus, the active microrheological methods often permit a direct measurement of the compliance  $J(t)$

$$\gamma(t) = \int_{-\infty}^t J(t-t') \dot{\sigma}(t') dt'. \quad (1.3)$$

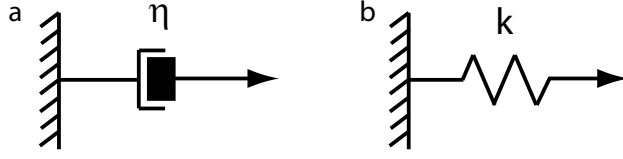


Figure 1.1: Fundamental elements for composition of mechanical circuits: dashpot with the viscosity  $\eta$  (a) and spring with the spring constant  $k$  (b).

The relaxation modulus can then be calculated through the convolution identity relating it to the compliance

$$\int_0^t G(t-t') J(t') dt' = t. \quad (1.4)$$

The basis of the active methods of microrheology is in extracting the storage and loss moduli by the simultaneous measurement of the applied force and the resulting displacement of the probe particle. Alternatively, the same information can be extracted from the observation of thermal fluctuations of the embedded particles as the fluctuation-dissipation theorem suggests [15].

The other frequently used way of interpreting the viscoelastic behavior is the description in terms of the so-called mechanical circuits composed of dashpots and springs [16], Fig. 1.1. These elements can be joined in parallel or in series producing various mechanical systems with different viscoelastic properties. The responses of these systems to an external force can be theoretically calculated and may be used for fitting the mechanical response of the medium under study. The significant disadvantage of this method is that a lot of elements might be required for a reasonable fit, which prevents from distinguishing between physical mechanisms responsible for the studied behavior.

### 1.3 Solutions of semiflexible polymers

Actin solutions are intensively studied by microrheology. Actin is a globular protein and is present in an enormous variety of biological species bearing different crucial functions, from structural to motile. Actin monomers self-assemble under appropriate conditions to form filaments with a diameter of 7 – 9 nm and lengths of up to 50  $\mu\text{m}$ .

One of the key motivations for the actin solutions to be a subject of constant microrheological studies is the prominent role of actin in the mechanical properties of cells. Actin is a building block of the cytoskeleton, which is responsible for the form maintenance of cells, and, therefore, their viscoelastic

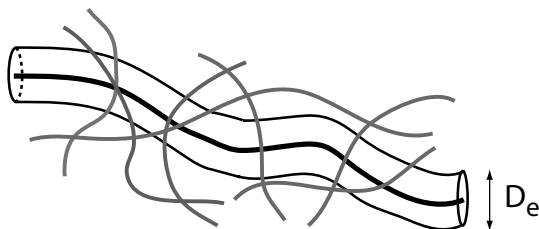


Figure 1.2: Reptation tube. The polymer is confined to an effective tube with diameter  $D_e$ , the walls of the tube are dynamically created by the neighboring fluctuating polymers.

properties. Furthermore, actin plays an important role in cell division and locomotion.

In addition to its important biological roles in cells, which draw constant interest to actin, it has become a prominent model of a semiflexible polymer. Filamentous actin possesses a persistence length of  $L_p = 17 \mu\text{m}$  [17, 18]. Therefore, in *in vitro* experiments the ratio of the average contour length  $L$  to the persistence length is intermediate between the limit of flexible polymers  $L/L_p \gg 1$  and a rod-like one  $L/L_p \ll 1$ . At appropriate salt concentration (physiological conditions) globular actin polymerizes to form isotropic entangled solutions of filamentous actin. Variation of the monomer actin concentration permits controlling the mesh size of the formed network and allows obtaining the tightly-entangled solutions in which the mesh size  $\xi$  is much smaller than the persistence length  $L_p$  [19].

Microrheological techniques allow testing different length and time scales in the actin solutions. Apart from the conventional microrheology, fluorescent labeling of single actin filaments permits real-time observation of their behavior in the actin solutions. Direct binding of micro- and nanoparticles to single actin filaments opens the possibilities of tracking the positions of the actin filaments as well as of enforced reptation experiments when a filament is pulled through the network [20, 21]. Actin solutions are thus very rich systems for rheological studies and pose challenging problems in the dynamics of cellular systems.

The presence of different length and time scales in the tightly-entangled semiflexible polymer solutions complicates their mechanical properties. Each polymer is assumed to be confined over certain times specified later to an effective dynamical tube with a diameter  $D_e \ll L_p$  [22], Fig. 1.2. The walls of the tube are dynamically created by collisions with other fluctuating polymers.

The tube is a consequence of the steric constraints present in such sys-

tems, which are responsible for the interesting mechanical behavior. Different time and length scales naturally appearing in the tube model of tightly-entangled polymer solutions are directly connected to various viscoelastic regimes observed in experiments.

Related to the width of the confinement tube is the entanglement (or deflection) length  $L_e$ , which can be interpreted as the distance between the collisions of the polymer with the walls of the tube. In the tightly-entangled regime the tube diameter and the entanglement length vary according to [23]

$$L_e \sim D_e^{2/3} L_p^{1/3}. \quad (1.5)$$

Different arguments lead to different dependencies of the tube width and the entanglement length on the polymer contour length density  $\rho$ , which is the ratio of the total contour length of all the polymers  $L_{\text{tot}}$  (i.e. the sum of the contour lengths of all polymers in the volume) to the volume of the system  $V$

$$\rho = \frac{L_{\text{tot}}}{V}. \quad (1.6)$$

Simple geometrical arguments [24] and the binary collision approximation [25] give the scaling

$$L_e \sim \rho^{-2/5} L_p^{1/5}, \quad D_e \sim \rho^{-3/5} L_p^{-1/5}, \quad (1.7)$$

while the effective medium approximation [25] gives the power laws

$$L_e \sim \rho^{-1/3} L_p^{1/3}, \quad D_e \sim \rho^{-1/2}. \quad (1.8)$$

### 1.3.1 High frequency viscoelasticity

Confined to an effective dynamical tube the polymer experiences shape fluctuations transversely to the tube as well as longitudinal Brownian motion. The width of the tube, which is dynamically created by fluctuating polymers, is orders of magnitude larger than the backbone diameter of the polymer, which is of the order of 10 nm, consequently on sufficiently short time scales the dynamics of the polymer is similar to the one of a free semiflexible polymer in solution. Such an approach is valid at times shorter than the typical time between successive collisions of the polymer with the walls of the tube. This time  $\tau_e$ , called also entanglement time, can be estimated as the relaxation time of the modes with wavelengths shorter than  $L_e$  [26]

$$\tau_e \sim \frac{\zeta_{\perp} L_e^4}{k_B T L_p}, \quad (1.9)$$

where  $\zeta_{\perp}$  is the friction coefficient for the perpendicular motion of the polymer,  $k_B$  is the Boltzmann constant and  $T$  is the temperature. Consequently, at frequencies  $\omega > \tau_e^{-1}$  the polymers in the solution can be regarded as free and the complex frequency dependent shear modulus may be shown to vary with frequency  $\omega$  as [26]

$$G^*(\omega) \sim \frac{\rho k_B T}{L_p} \left( i\omega \frac{\zeta_{\perp} L_p^3}{k_B T} \right)^{3/4}, \quad (1.10)$$

which is a direct consequence of the finite rigidity of the actin filaments. Thus, the storage and the loss moduli  $G'(\omega)$  and  $G''(\omega)$  both vary with the frequency as  $\omega^{3/4}$ . In the time domain this power law corresponds to the dependence of the relaxation modulus on time

$$G(t) \sim t^{-3/4} \quad (1.11)$$

at times  $t \lesssim \tau_e$ . The power law dependence on frequency 1.10 has been found experimentally by a number of researchers [8, 20, 27–30] in passive as well as in active microrheology of actin solutions.

The study [8] comprises a set of active and passive microrheological experiments on the actin polymer networks with the mesh size  $\xi \approx 1 \mu\text{m}$ . It is shown that the beads with the diameter  $d$  smaller than the mesh size exhibit usual Brownian diffusion  $\langle x^2(t) \rangle \sim t$ , where  $x(t)$  is the coordinate of the bead's center of mass. It means that the movement of the small beads is weakly influenced by the polymer network and the beads are able to diffuse freely. On the contrary, beads larger than the mesh size show the mean square displacement scaling as

$$\langle x^2(t) \rangle \sim t^{3/4}. \quad (1.12)$$

When an external force is applied on the bead with the diameter  $d/\xi \sim 3$  its displacement is given by the power law

$$x(t) \sim t^{3/4} \quad (1.13)$$

The power laws 1.12 and 1.13 are related to the  $\omega^{3/4}$  high frequency scaling 1.10 of the complex relaxation modulus  $G^*(\omega)$  and were observed at times  $t \lesssim 2 \text{ sec}$  [8].

Passive microrheology studies of actin solutions with the  $5 \mu\text{m}$  beads, which are about 20 times larger than the mesh size as well show the scaling 1.10 for frequencies above 10 Hz [28].

Summarizing, extensive experimental data reveals the  $\omega^{3/4}$  scaling of both the storage  $G'(\omega)$  and the loss  $G''(\omega)$  moduli at frequencies  $\omega > \tau_e^{-1}$  with  $\tau_e$  being in accord with the estimate 1.9.

### 1.3.2 Elastic plateau

Whereas there is a significant agreement between the theoretical predictions and various experimental observations on the high frequency viscoelastic response of the semiflexible polymer solutions, the experimental data at frequencies below  $\tau_e^{-1}$  deviate from one research group to another. It is generally assumed [26, 31] that solutions of semiflexible polymers exhibit elastic behavior at times  $\tau_e < t < \tau_{\text{rep}}$ , where  $\tau_{\text{rep}}$  is the so-called reptation time a polymer requires to disengage from its tube by longitudinal diffusion (reptation) [22]. This regime is characterized by a plateau in the time dependence of the relaxation modulus  $G(t)$  at times  $\tau_e < t < \tau_{\text{rep}}$ . Accordingly, in the frequency domain the storage modulus  $G'(\omega)$  as well experiences a plateau at frequencies  $\tau_{\text{rep}}^{-1} < \omega < \tau_e^{-1}$ , whereas the loss modulus  $G''(\omega)$  shows a minimum in this frequency range being much smaller than the storage modulus  $G'(\omega) \gg G''(\omega)$ , which is a signature of an elastic behavior. The value of the plateau modulus  $G_{\text{pl}}$  is defined as the value of the storage modulus at the frequency where the loss modulus  $G''(\omega)$  experiences a local minimum.

A broad elastic plateau measured using the diffusing wave spectroscopy technique has been reported in an actin solution with the mesh size  $\xi \approx 0.15 \mu\text{m}$ , in which microspheres with the diameter  $0.96 \mu\text{m}$  were embedded [29, 30, 32]. The plateau with the value of about 1.4 Pa spanned a frequency range of several orders of magnitude  $10^{-3} < \omega < 10^1 \text{ Hz}$ . Other studies [33] report a significantly higher plateau modulus of over 10 Pa in the frequency range  $10^{-2} < \omega < 10^2 \text{ Hz}$  as well as much lower values of the order of 0.1 Pa [34].

The origin of the elastic plateau is considered to be in the forces resisting the transverse deformations of the conformations of the tubes [35]. This mechanism is expected to give

$$G_{\text{pl}} \sim \frac{k_{\text{B}}T}{L_e \xi^2}. \quad (1.14)$$

At frequencies even lower than  $\tau_{\text{rep}}^{-1}$  the viscoelastic behavior is believed [26, 31] to be similar to that of a viscous fluid. Therefore, at frequencies  $\omega \ll \tau_{\text{rep}}^{-1}$  the storage and the loss moduli scale as  $G'(\omega) \sim \omega^2$  and  $G''(\omega) \sim \omega$ . The reptation time takes the values of 1000 s and longer as suggested by the experiments [32, 34].

Thus, schematically the real and the imaginary parts of the complex modulus  $G^*(\omega)$  vary with the frequency as sketched in the Fig. 1.3. In the time domain the relaxation modulus  $G(t)$  corresponding to the complex modulus from the Fig. 1.3 is sketched in the Fig. 1.4a. The respective time dependence of the compliance  $J(t)$ , which can be found solving the convolution identity

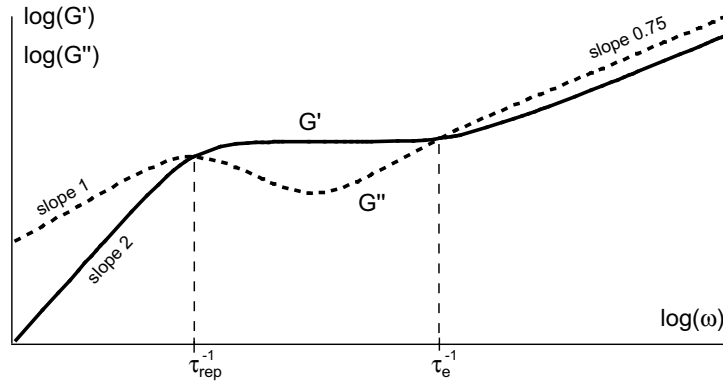


Figure 1.3: A sketch of the storage  $G'$  (solid line) and the loss  $G''$  (dashed line) moduli as functions of frequency. At high frequencies  $\omega \gg \tau_e^{-1}$  both moduli exhibit a power law  $\omega^{0.75}$ , at intermediate frequencies  $\tau_{\text{rep}}^{-1} \ll \omega \ll \tau_e^{-1}$  an elastic plateau is found, and at low frequencies  $\omega \ll \tau_e^{-1}$  a viscous flow scaling takes place  $G'(\omega) \sim \omega^2$  and  $G''(\omega) \sim \omega$ .

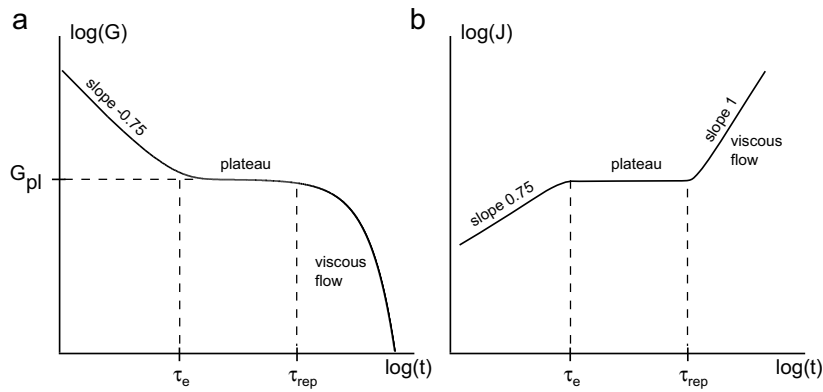


Figure 1.4: Sketches of the time dependent relaxation modulus  $G(t)$  (a) and the compliance  $J(t)$  (b) corresponding to the complex modulus  $G^*(\omega)$  from the Fig. 1.3.

Eq. 1.4, is sketched in the Fig. 1.4b.

The differences of 2 orders of magnitude in the reported values of the plateau modulus as well as in the frequency range spanned by the plateau regime suggest that this can be due to the presence of cross-linkage between the filaments [27, 31]. A small uncontrolled quantity of proteins, which can act as chemical cross-links, can dramatically change the viscoelastic properties of an actin solution. This point of view is confirmed by the study [36] showing that the viscoelastic properties of actin filament networks strongly depend on the history of the sample.

Apart from the behavior shown in the Figs. 1.3 and 1.4 there exist studies that report different dependence of the complex modulus  $G^*(\omega)$  on frequency at frequencies  $\omega < \tau_e^{-1}$ . No elastic plateau is observed in [28] within the experimentally studied frequency window up to frequencies as low as 0.1 Hz. This study reports results of passive microrheology of actin filament solutions with the mesh size of  $\xi \approx 0.2 \mu\text{m}$  using the  $5 \mu\text{m}$  beads, which are, therefore, about 20 times larger than the mesh size. Whereas the complex modulus  $G^*(\omega)$  shows the usual  $\omega^{0.75}$  scaling at frequencies above 10 Hz, in the frequency range  $0.1 < \omega < 10$  Hz it varies as  $\omega^\alpha$  with a lower exponent  $0.5 < \alpha < 0.75$ . The exponent  $\alpha = 0.5$  was found by the two-point microrheology in the frequency range  $0.4 < \omega < 80$  Hz [5].

### 1.3.3 Recent active microrheological experiments on actin solutions

Recent active microrheological studies of actin networks are in accord with the  $\omega^{0.5}$  scaling of the complex modulus  $G^*(\omega)$  in the frequency range  $0.1 \lesssim \omega \lesssim 10$  Hz [37]. This treatise describes a set of experiments on enforced motion of a microbead in actin solutions using a magnetic tweezers setup. The advantage of these experiments with respect to the earlier ones [38] with a similar setup is that the spatial resolution, the time resolution as well as the possible duration of the applied force pulses have been improved by an order of magnitude. The mesh size of the studied networks was 10 to 20 times smaller than the diameter of the microbeads  $4.5 \mu\text{m}$ .

The main results can be formulated as follows. Three distinct regimes are found in the time dependence of the compliance  $J(t)$ , which is proportional to the displacement of the bead  $x(t)$ . These regimes can be represented as power laws

$$J(t) \approx A_i t^{\alpha_i}, \quad (1.15)$$

where the exponents  $\alpha_i$  take the values:

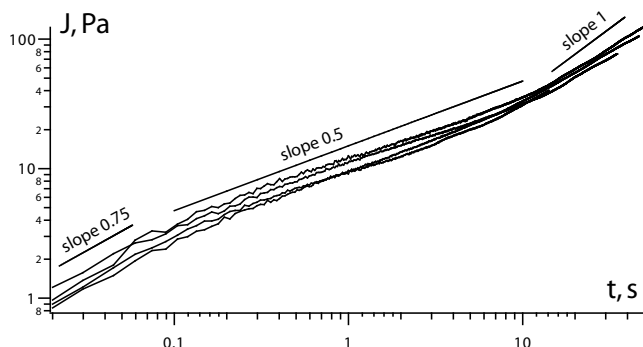


Figure 1.5: Compliance of actin networks as measured in active microrheological experiments [37]. With a kind permission of Jörg Uhde.

- In the initial regime at times  $0 < t < \tau_1$ , where  $\tau_1 \approx 0.3$  s, the exponent takes the value  $\alpha_1 = 0.75$
- In the intermediate regime spanning the time window  $\tau_1 < t < \tau_2$ , where  $\tau_2 \approx 10$  s, a square root time dependence of the compliance is found  $\alpha_2 = 0.5$
- The intermediate regime is followed at times  $t > \tau_2$  by the viscous-like motion with the exponent taking the values  $\alpha_3 \approx 1$ .

Some typical measured compliances of the actin networks are shown in the Fig. 1.5. Furthermore, it is found that the amplitude  $A_2$  of the square root regime is force dependent  $A_2 \sim f^{-0.25}$  and that it varies with the concentration  $c$  of polymers as  $A_2 \sim c^{-1.3}$ .

The described results can not be interpreted using mechanical circuits composed of the dashpots and springs shown in the Fig. 1.1 as it has been done in [38].

The behavior of the compliance shown in the Fig. 1.5 is not in accord with the relaxation modulus shown in the Fig. 1.3. As we assert in the Ch. 5 instead of the plateau both the storage and the loss moduli experience  $\omega^{0.5}$  scaling in the frequency range corresponding to the square root dependence of the compliance on time. The latter scaling was observed for the first time in the active microrheology. The power law  $G^* \sim \omega^{0.5}$  has been predicted theoretically for polymer networks with  $L/L_p \gg 1$  by accounting for the diffusion of the excess length of the filaments [26, 31]. In actin networks  $L/L_p \approx 1.2$  and therefore, this mechanism is not expected to manifest itself over two decades as observed in experiments [37].

In this work we study theoretically the active microrheology of the entangled semiflexible polymer networks aiming to understand the origin and

peculiarities of the square root regime. We first simulate the enforced motion of the bead through the network. The simulations enable us to model the experiments as well as to establish scaling relations between the parameters of the system. On the basis of these results we then propose a new mechanism of the response of the network to the bead motion and develop an analytical scaling theory.

## Chapter 2

# Computer simulation of polymer networks microrheology

Rapid development of computational power facilitates the use of numerical methods in a great number of fields where the analytical models are ill-developed or fail due to the complexity of the geometry. Our aim is to gain insight into the microrheology of solutions of filamentous proteins as well as to study the diffusional properties of semiflexible polymers in solutions.

A great number of methods is concerned with predicting hydrodynamic behavior of complex systems (fluids). The traditional methods of solving partial differential equations meet only limited success, therefore favoring the use of different molecular dynamics methods. Rapid development of various kinds of molecular dynamics methods opens great possibilities for studies of not only microscale systems but provides wide opportunities in tackling mesoscopic problems.

The simulation of polymer networks and all the more of the microrheology of such objects is a difficult task due to the complexity of the system manifesting itself in the presence of different time and length scales. The time scales relevant to the viscoelastic behavior range from below the characteristic time  $\tau_e$  for a chain to explore the tube to the characteristic time  $\tau_{\text{rep}}$  and longer for the chain to disengage from the tube by reptation, Ch. 1. At the same time characteristic length scales for actin range from  $\approx 0.1 \mu\text{m}$  which is a typical mesh size to  $\approx 20 \mu\text{m}$  which is of the order of the persistence length [17, 18]. Such a wide range of length and time scales makes it difficult to perform any microscopic simulation due to very big number of objects which would then have to be taken into consideration and a small time step because of the strongly varying interaction potentials. Therefore

some sort of coarse-grained technique has to be used. One of such techniques is the dissipative particle dynamics method introduced a decade ago.

## 2.1 The dissipative particle dynamics method

The dissipative particle dynamics (DPD) method introduced by Hoogerbrugge and Koelman [39] is a rapidly developing promising technique for the simulation of hydrodynamic behavior. The DPD system can be imagined as bridging the gap between microscopic simulation methods such as molecular dynamics and macroscopic approaches involving the solution of the fluid flow equations. This method can be understood as a coarse-graining of the fluid particles on the physically significant length scale so that all smaller scale motions are ignored. Alternatively, DPD can be interpreted as a stochastic description of the macroscopic differential fluid equations on a smaller length scale [40]. The thermodynamics of the model has much in common with the Langevin approach, being its generalization where the presence of two-particle interactions results in the addition of hydrodynamics.

The DPD approach enables one to obtain a correct hydrodynamic behavior [41–43]. On the length scales larger than the particle interaction range the system is completely described by the hydrodynamic equations, i.e. the Navier-Stokes limit is recovered.

The DPD method has been successfully applied to a number of systems. It has been used to study the liquid-vapor coexistence [44], to simulate the colloidal particle scattering and aggregation in colloids [45], and to study the phase separation in immiscible fluids [46]. The DPD method has been successfully applied to study the spontaneous aggregation of amphiphiles into bilayers, determination of their equilibrium properties and measuring of the surface tension and the bending rigidity of the bilayers [47, 48], as well as to study the spontaneous vesicle formation [49]. Electrostatic interactions were incorporated in the DPD method and the modified model was applied to polyelectrolyte solutions [50].

Shortly after its creation the DPD method has been recognized to be well-suited for the simulation of polymer systems and has been applied to study polymer solutions. The studies comprise polymer-solvent phase separation and the influence of branching [51, 52], effects of the solvent quality on the conformation and relaxation of polymers [53], block copolymer microphase separation [54]. Scaling laws for polymers in the DPD method were checked in dilute solutions as well as in polymer melts and a good agreement with the predictions was found [55, 56].

## 2.2 Constituent equations

Each DPD particle is represented by a sphere possessing a mass. Its time evolution is governed by Newton's equations of motion

$$\frac{d\mathbf{r}_{\alpha i}}{dt} = \mathbf{v}_{\alpha i}, \quad m_{\alpha} \frac{d\mathbf{v}_{\alpha i}}{dt} = \mathbf{f}_{\alpha i}, \quad (2.1)$$

where Greek letters refer to the sort of the particle, while the Latin ones refer to the number of the particle within a sort. For our simulations we utilized three sorts of particles: the bead, the water spheres and the monomer spheres. All interactions are pairwise and include a conservative force  $\mathbf{F}^C$ , a dissipative force  $\mathbf{F}^D$  and a random force  $\mathbf{F}^R$

$$\mathbf{f}_{\alpha i} = \sum_{\beta, j} (\mathbf{F}_{\alpha\beta ij}^C + \mathbf{F}_{\alpha\beta ij}^D + \mathbf{F}_{\alpha\beta ij}^R), \quad (2.2)$$

where  $(\beta, j) \neq (\alpha, i)$ . All interactions except for the persistence and spring forces, which will be introduced later, possess cutoff lengths depending on the radii  $R_{\alpha}$  of the interacting particles. The conservative force is a soft repulsion acting along the line of centers

$$\mathbf{F}_{\alpha\beta ij}^C = \begin{cases} a_{\alpha\beta} \left(1 - \frac{r_{\alpha\beta ij}}{R_{\alpha} + R_{\beta}}\right) \hat{\mathbf{r}}_{\alpha\beta ij}, & r_{\alpha\beta ij} < R_{\alpha} + R_{\beta} \\ 0, & r_{\alpha\beta ij} \geq R_{\alpha} + R_{\beta} \end{cases}, \quad (2.3)$$

where  $a_{\alpha\beta}$  is a maximum repulsion between the particles of sorts  $\alpha$  and  $\beta$ ,  $\mathbf{r}_{\alpha\beta ij} = \mathbf{r}_{\alpha i} - \mathbf{r}_{\beta j}$ ,  $r_{\alpha\beta ij} = |\mathbf{r}_{\alpha\beta ij}|$ ,  $\hat{\mathbf{r}}_{\alpha\beta ij} = \mathbf{r}_{\alpha\beta ij} / |\mathbf{r}_{\alpha\beta ij}|$ . The remaining two forces are a dissipative or drag force and a random force. They are given by

$$\mathbf{F}_{\alpha\beta ij}^D = -\gamma_{\alpha\beta} w^D \left( \frac{r_{\alpha\beta ij}}{R_{\alpha} + R_{\beta}} \right) (\hat{\mathbf{r}}_{\alpha\beta ij} \cdot \mathbf{v}_{\alpha\beta ij}) \hat{\mathbf{r}}_{\alpha\beta ij} \quad (2.4)$$

$$\mathbf{F}_{\alpha\beta ij}^R = \sigma_{\alpha\beta} w^R \left( \frac{r_{\alpha\beta ij}}{R_{\alpha} + R_{\beta}} \right) \theta_{\alpha\beta ij} \hat{\mathbf{r}}_{\alpha\beta ij},$$

where  $\gamma_{\alpha\beta}$  and  $\sigma_{\alpha\beta}$  are respectively the dissipative and random force constants,  $w^D$  and  $w^R$  are r-dependent weight functions specified below,  $\mathbf{v}_{\alpha\beta ij} = \mathbf{v}_{\alpha i} - \mathbf{v}_{\beta j}$ , and  $\theta_{\alpha\beta ij}(t)$  is a randomly fluctuating variable with the Gaussian statistics

$$\begin{aligned} \langle \theta_{\alpha\beta ij}(t) \rangle &= 0 \\ \langle \theta_{\alpha\beta ij}(t) \theta_{\alpha'\beta' i' j'}(t') \rangle &= (\delta_{\alpha\alpha'} \delta_{ii'} \delta_{\beta\beta'} \delta_{jj'} + \\ &\quad \delta_{\alpha\beta'} \delta_{i j'} \delta_{\beta\alpha'} \delta_{j i'}) \delta(t - t'). \end{aligned} \quad (2.5)$$

The dissipative and random forces 2.4 also act along the line connecting the centers of the spheres and conserve linear and angular momentum. There is an independent random function  $\theta_{\alpha\beta ij}(t)$  for each pair of particles.

On the basis of the fluctuation dissipation theorem [57] it was shown that one of the two weight functions appearing in Eqs. 2.4 can be chosen arbitrarily and that this choice fixes the other weight function as well as that the amplitudes of the random and dissipative forces are related to  $k_B T$  as

$$w^D(r) = [w^R(r)]^2, \quad \sigma_{\alpha\beta}^2 = 2\gamma_{\alpha\beta} k_B T. \quad (2.6)$$

Following [58] we take

$$w^D(r) = [w^R(r)]^2 = \begin{cases} (1-r)^2, & r < 1 \\ 0, & r \geq 1 \end{cases}. \quad (2.7)$$

For the iteration scheme we use a modified version of the velocity-Verlet algorithm to advance the set of positions and velocities of the particles [58, 59]

$$\begin{aligned} \mathbf{r}_{\alpha i}(t + \Delta t) &= \mathbf{r}_{\alpha i}(t) + \Delta t \mathbf{v}_{\alpha i}(t) + (\Delta t)^2 \frac{\mathbf{f}_{\alpha i}(t)}{2m_{\alpha}}, \\ \tilde{\mathbf{v}}_{\alpha i}(t + \Delta t) &= \mathbf{v}_{\alpha i}(t) + \Delta t \frac{\mathbf{f}_{\alpha i}(t)}{2m_{\alpha}}, \\ \mathbf{f}_{\alpha i}(t + \Delta t) &= \mathbf{f}_{\alpha i}(\mathbf{r}(t + \Delta t), \tilde{\mathbf{v}}(t + \Delta t)), \\ \mathbf{v}_{\alpha i}(t + \Delta t) &= \mathbf{v}_{\alpha i}(t) + \Delta t \frac{\mathbf{f}_{\alpha i}(t) + \mathbf{f}_{\alpha i}(t + \Delta t)}{2m_{\alpha}}, \end{aligned}$$

where  $\Delta t$  is the time step of the iteration. The random force takes the form [58]

$$\mathbf{F}_{\alpha\beta ij}^R = \sigma_{\alpha\beta} w^R \left( \frac{r_{\alpha\beta ij}}{R_{\alpha} + R_{\beta}} \right) \zeta_{\alpha\beta ij} \Delta t^{-1/2} \hat{\mathbf{r}}_{\alpha\beta ij}, \quad (2.8)$$

where  $\zeta_{\alpha\beta ij}$  is a random number with zero mean and unit variance chosen independently for each pair of interacting particles at each time step.

## 2.3 Polymer model

We utilize the bead-and-spring model [22] for the connection of monomers into polymers. Therefore, a spring force acts between two adjacent monomers. The spring force acting on a monomer ( $\alpha i$ ) from the adjacent monomer ( $\alpha j$ ) is given by

$$\mathbf{F}_{\alpha\alpha ij}^S = -k(r_{\alpha\alpha ij} - d)\hat{\mathbf{r}}_{\alpha\alpha ij}, \quad (2.9)$$

where  $k$  is the spring constant, and  $d$  is the equilibrium bond length.

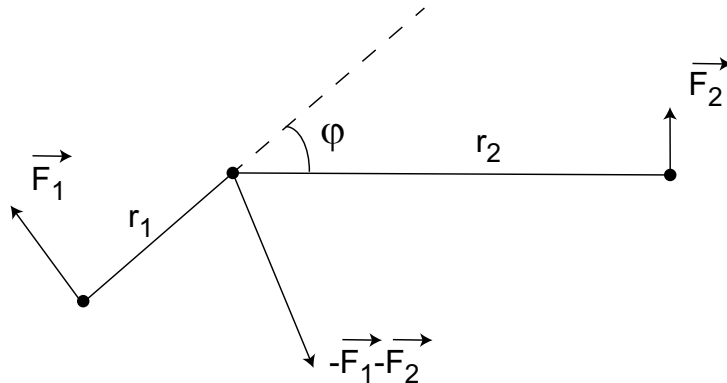


Figure 2.1: Persistence forces. The forces  $\vec{F}_1$  and  $\vec{F}_2$  act on the monomers 1 and 2 and are normal to the bonds 1-3 and 2-3, respectively. The force  $\vec{F}_3$  acting on the monomer 3 is opposite to the vector sum  $\vec{F}_1 + \vec{F}_2$ .

Our aim is the simulation of solutions of semiflexible polymers, therefore, we introduce forces providing persistence of the polymers as depicted in the Fig. 2.1. The absolute values of the forces  $\vec{F}_1$  and  $\vec{F}_2$  are

$$F_1 = \frac{\mu\varphi}{r_1}, \quad F_2 = \frac{\mu\varphi}{r_2}, \quad (2.10)$$

where  $r_1$  and  $r_2$  are the lengths of the bonds 1-3 and 2-3, respectively, and  $\mu$  is the force constant. Such a choice of the forces  $\vec{F}_1$  and  $\vec{F}_2$  implies that the torques they exert on the monomer 3 compensate each other. Together with the choice  $\vec{F}_3 = -\vec{F}_1 - \vec{F}_2$  that the total force acting on the trimer is zero it implies that the total torque of these forces with respect to any point in space is also zero. Such a choice of forces favors the straight configuration with  $\varphi = 0$ , therefore introducing persistence to the polymers. The persistence length can be varied by changing the force constant  $\mu$ .

## 2.4 Simulation box and boundary conditions

If one could have a simulation box with solid sides, which is orders of magnitude bigger than the biggest typical length scale in the system, e.g. the contour or the persistence length of the polymers, it would resemble the situation met in the *in vitro* experiments: polymer solution in a chamber with the beads embedded. The time, which is required for a computer to make a single time step of the simulation, grows only linearly with the volume of the simulation box, owing to the presence of the cutoff distances for all interaction forces in the system. In spite of this linear scaling, the present

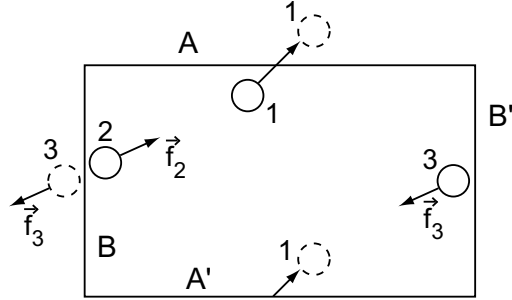


Figure 2.2: Boundary conditions in the simulation box. The objects are allowed to go through the walls appearing on the opposite side (the object 1 goes through the wall  $A$  and appears on the other side near the wall  $A'$ ), and interact through a wall if they are within the interaction distance (the object 2 near the wall  $B$  interacts with the object 3 near the wall  $B'$ ).

computer facilities, unfortunately, let us simulate systems, which are only few times larger than the bead size. On the other hand, performing the simulations in such a small solid box would introduce uncontrolled influence of the solid walls of the box on the system. It would influence the viscosity of the system because the hydrodynamics near a wall is different than that in the bulk. Furthermore, it would as well force the polymers to bend near the walls influencing their conformations. In order to avoid these problems we introduce the following three properties of the simulation box. (i) we utilize periodic boundary conditions by making the opposite sides of the simulation box equivalent.

The DPD simulation of the semiflexible polymer solution is performed in a three-dimensional box with dimensions  $L_x$ ,  $L_y$  and  $L_z$  filled with water spheres, monomer spheres, which are connected into polymers as specified in the sec. 2.3, and a bead. All polymers possess the same contour length, which is chosen as to not exceed the smallest dimension of the simulation box. All the opposite walls of the box are made equivalent, therefore objects going away through a wall enter the box from the opposite side, see Fig. 2.2. Furthermore, the objects are allowed to interact through the walls if they are within the cutoff distance, the objects 1 and 2 in the Fig. 2.2.

Such a choice of the boundary conditions ensures that the polymers are not influenced by the walls. On the other hand, the contour length of the simulated polymers is shorter than the smallest dimension of the simulation box, which provides the absence of the spurious self interaction of polymers, Fig. 2.3.

In the simulations an external force is applied on the bead embedded in

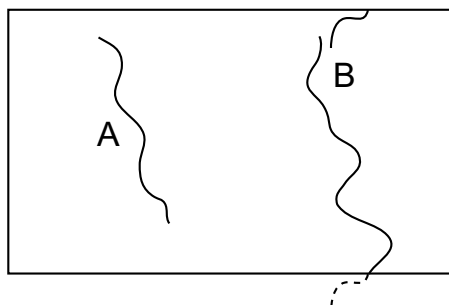


Figure 2.3: The contour length of the simulated polymers is shorter than the smallest dimension of the wall (polymer A) in order to prevent the possible spurious self interaction of the polymers (polymer B in the picture).

the solution of semiflexible polymers. This causes the bead's displacement, which is then analyzed. The intrinsic peculiarity of the DPD method is that all interactions are pair-wise providing the conservation of linear momentum. The simulations are initialized in a state with zero total momentum and with a Maxwell-Boltzmann velocity distribution appropriate to the temperature of the simulation. In the absence of an external force, the total linear momentum remains zero. In the case when an external force is applied, however, the total linear momentum of the system increases, which means that the entire system moves. Therefore, the movement of the system's center of mass also contributes to the displacement of the bead. To avoid this spurious contribution we implement the second property of the simulation box (ii) introducing non-slip boundary conditions for water spheres near the walls of the simulation box parallel to the external force applied on the bead, Fig. 2.4. The components of the velocities of all water spheres in a thin layer near the walls, which are parallel to them, are explicitly put to zero at every iteration step. Finally, the third property of the simulation box (iii) is that the non-slip boundary conditions do not apply to the monomers in order not to freeze the whole system.

## 2.5 Active microrheology of semiflexible polymer solutions

Our goal is to simulate the microrheology of the tightly entangled semiflexible polymer solutions. In order to obtain reliable results characteristic features of such microrheological experiments have to be in line with the simulations. These are, first of all, the length scales met in the experiments, which form

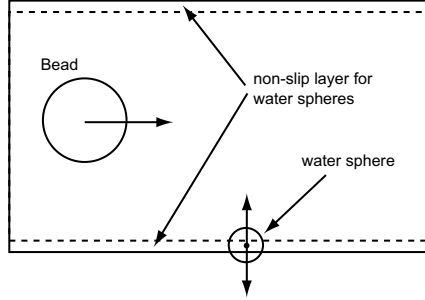


Figure 2.4: Thin non-slip layers near the walls parallel to the direction of the application of the external force on the bead. The water spheres in the layers are only able to move perpendicular to them.

a certain hierarchy that has to be preserved. Therefore, the mesh size of the simulated polymer network is approximately one order of magnitude smaller than the diameter of the bead, which probes the viscoelastic properties of the medium. It, thus, resembles the experiments on filamentous actin solutions when the mesh size is of the order of  $0.5 \mu\text{m}$ , whereas the diameter of the probing bead is of the order of  $5 \mu\text{m}$ . The size of the bead in the simulations is few times smaller than the length of the polymers, which as well meets the experimental conditions where the average actin filament length is  $10\text{--}20 \mu\text{m}$ . The persistence length of the filamentous actin is  $17 \mu\text{m}$  and that of the polymers in the simulations is also of the order of their contour length.

It has to be noted that in the simulations all quantities such as, for example, the dimensions of the simulation box, the simulation time or the interaction constants are in arbitrary simulation units. The simulations are performed in a 3-dimensional box with dimensions  $L_x = 40$ ,  $L_y = 80$  and  $L_z = 40$  units, which is filled with water spheres with radius  $R_w = 0.8$ , monomer spheres with radius  $R_m = 0.3$  and a bead with the radius  $R_b = 10$ . The  $L_y$  dimension is taken to be bigger than  $L_x$  and  $L_z$ , because the external force on the bead will be applied along the  $Oy$  axis. Following [58], the number density of water spheres, which is the ratio of the number of water spheres in the simulation box to its volume, is chosen to be 3 and the repulsion parameter  $a_{ww}$  of the conservative force 2.3 for water-water interaction is chosen  $a_{ww} = 45$  in order for the compressibility of the DPD fluid to be close to that of water [58]. The dissipative force constant  $\gamma_{ww}$ , Eqs. 2.4, of the water-water interaction is  $\gamma_{ww} = 1$ , this choice fixes the random force constant through the Eqs. 2.6.

Each polymer is composed of 70 monomers, which are connected by massless harmonic springs acting between two adjacent monomers, Eq. 2.9. The

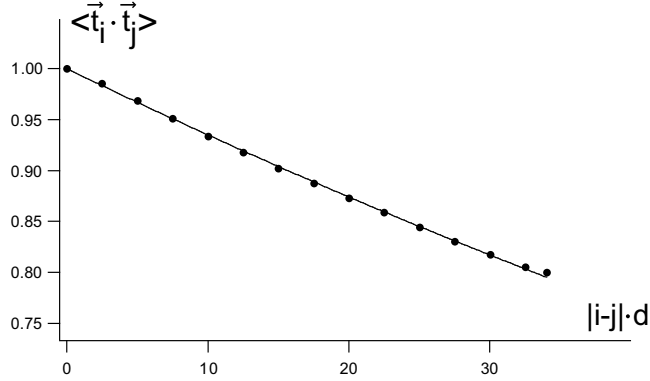


Figure 2.5: The calculated correlation function  $\langle \mathbf{t}_i \cdot \mathbf{t}_j \rangle$  (data points) and fitting (solid line), Eq. 2.11, with  $L_p = 150$ .

bond length is  $d = 0.5$  and the polymers are, therefore, 34.5 units long. The spring constant is  $k = 400$ . The bond length  $d$  is shorter than the diameter of the monomers  $2R_m = 0.6$ , which prevents bonds from crossing each other and provides, therefore, the topological constraints present in polymer systems. Furthermore, the chosen value of the spring constant provides that the number of bonds longer than the diameter of the monomer is less than 2% of the total number of bonds, which has been checked during our simulations.

Persistence forces are added as described in the Sec. 2.3 and the persistence force constant is  $\mu = 385$ , which gives a persistence length of approximately  $L_p = 150$  units. To obtain this value of the persistence length out of our simulations the correlation function  $\langle \mathbf{t}_i \cdot \mathbf{t}_j \rangle$  is calculated, where  $\mathbf{t}_i$  is the unit vector directed from the monomer  $i$  to the monomer  $i + 1$  of the same polymer. This correlation function decays according to [15]

$$\langle \mathbf{t}_i \cdot \mathbf{t}_j \rangle = \exp\left(-\frac{|i-j| \cdot d}{L_p}\right), \quad (2.11)$$

which allows to obtain the persistence length by the fitting procedure. The calculated correlation function and the fitting with  $L_p = 150$  are showed in the Fig. 2.5 (see also Fig. 2.7).

The monomer-monomer conservative force constant is  $a_{mm} = 35$  and the dissipative one is  $\gamma_{mm} = 5$ . The monomer-water conservative force constant is  $a_{mw} = 0$  and the dissipative one is  $\gamma_{mw} = 1$  unless specified. The masses of the water and monomer spheres are  $m_w = 0.0001$  and  $m_m = 0.0001$ .

The mass of the bead is  $m_b = 1$  and the force constants for the bead-water and bead-monomer interactions are chosen to be  $a_{bw} = 550$ ,  $a_{bm} = 550$ ,  $\gamma_{bw} = 0.1$  and  $\gamma_{bm} = 0.1$ .

Table 2.1: Parameters of the DPD model used for simulating active microrheology of semiflexible polymer solutions

Parameter	$L_x$	$L_y$	$L_z$	$R_b$	$R_m$	$R_w$
Value	40	80	40	10	0.3	0.8
Parameter	$a_{ww}$	$\gamma_{ww}$	$a_{mm}$	$\gamma_{mm}$	$a_{mw}$	$\gamma_{mw}$
Value	45	1	35	5	0	1
Parameter	$a_{bw}$	$\gamma_{bw}$	$a_{bm}$	$\gamma_{bm}$	$k_B T$	$\Delta t$
Value	550	0.1	550	0.1	1	0.00005
Parameter	$m_b$	$m_w$	$m_m$	$d$	$k$	$\mu$
Value	1	0.0001	0.0001	0.5	400	385

The time step in the simulations is 0.00005, which provides good temperature control. The temperature has been controlled by monitoring the mean kinetic energy of the monomer and water spheres, which was to an accuracy of approximately 2% equal to  $3k_B T/2$ . In all simulations we choose  $k_B T = 1$ . The parameters of the simulation model are summarized in the Tab. 2.1

### 2.5.1 Enforced movement of the bead in pure water

In order that the microrheology simulations be reliable, the hydrodynamics of the simulated water by the dissipative particle dynamics should be close to that of a real fluid. To check this simulation of the enforced movement of the bead in pure water has been performed.

The velocity of a spherical particle  $v(t)$  as a function of time  $t$  moving under a constant applied force  $f$  from the state with zero velocity  $v(0) = 0$  is given by

$$v(t) = \frac{f}{g} \left( 1 - \exp\left(-\frac{g}{m}t\right) \right), \quad (2.12)$$

which is the solution of the equation  $m\dot{v}(t) + gv(t) = f$ , where the dot indicates a time derivative,  $m$  is the mass of the particle and  $g$  is a viscous drag coefficient (for a sphere of radius  $R$  in an infinite fluid  $g = 6\pi R\eta$ , where  $\eta$  is the viscosity of the fluid). Velocity of the bead as a function of time in a simulation with  $f = 1000$  applied at  $t = 0$  parallel to the Oy axis is shown in the Fig. 2.6a by the dotted line. The mass and the radius of the bead were taken  $m = 1$ ,  $R = 10$  as specified above. The solid line in the Fig. 2.6a is

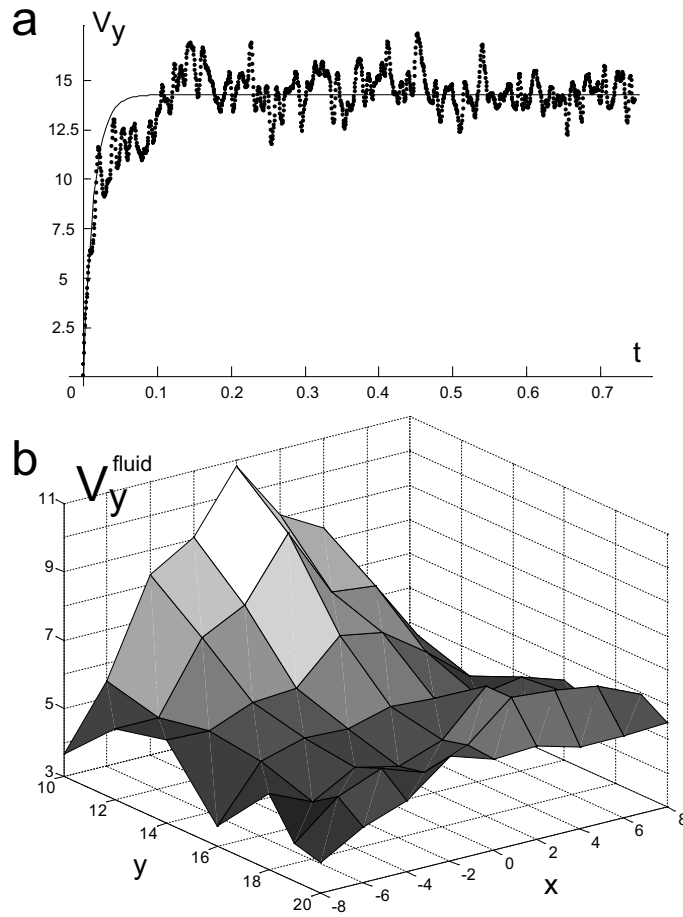


Figure 2.6: (a) Velocity of the bead as a function of time moving under an applied force  $f = 1000$  at  $t = 0$  (dotted line). The solid line is a fit by the dependence Eq. 2.12 with  $m = 1$ . The value of  $g$  obtained by the fitting is  $g = 70.06$ . (b) The distribution of the fluid velocity component parallel to the external force in front of the bead. The coordinate origin is in the center of the bead and the  $z = 0$  section is shown.



Figure 2.7: A polymer composed of 70 monomers as simulated by the DPD method.

a fit with the help of the Eq. 2.12. The value of  $g$  obtained by the fitting is  $g = 70.06$ . It follows from the Eq. 2.12 that the bead accelerates within the characteristic time  $\tau_{\text{acc}} = m/g \approx 0.015$ , which is the characteristic time of the inertial motion. At times  $t > \tau_{\text{acc}}$  the bead reaches on average a steady velocity. Since the characteristic time  $\tau_{\text{acc}}$  is two orders of magnitude shorter than the typical simulation time we will not discuss the inertial regime of the motion of the bead further on.

The Fig. 2.6b depicts the velocity component parallel to the externally applied force of the fluid in front of the moving bead. The data is represented in a coordinate system with the origin in the center of the bead. The force is applied along the Oy axis and the  $z = 0$  section is shown. The data are averaged over the time window  $t \in [0, 0.7]$ .

### 2.5.2 Responses of the bead on external forces

The number of time steps in a typical simulation was of the order of 100000, which required 1 to 2 months of the CPU time of a personal workstation. Therefore, a typical simulation spans a time window of about 5 time units. Depending on the applied force, during such a simulation time the bead displaces over a distance comparable to its radius.

A polymer composed of 70 monomers and possessing a contour length of about 34.5 units is shown in the Fig. 2.7. During the simulations a bead moves in a solution of such polymers under an applied constant external force, Fig. 2.8. At the moment of the application of the external force  $t_a$  the polymers are homogeneously distributed around the bead, Fig. 2.8a. At times  $t_c > t_b > t_a$  the bead displaces in the direction of the force deforming the network, Figs. 2.8b and 2.8c.

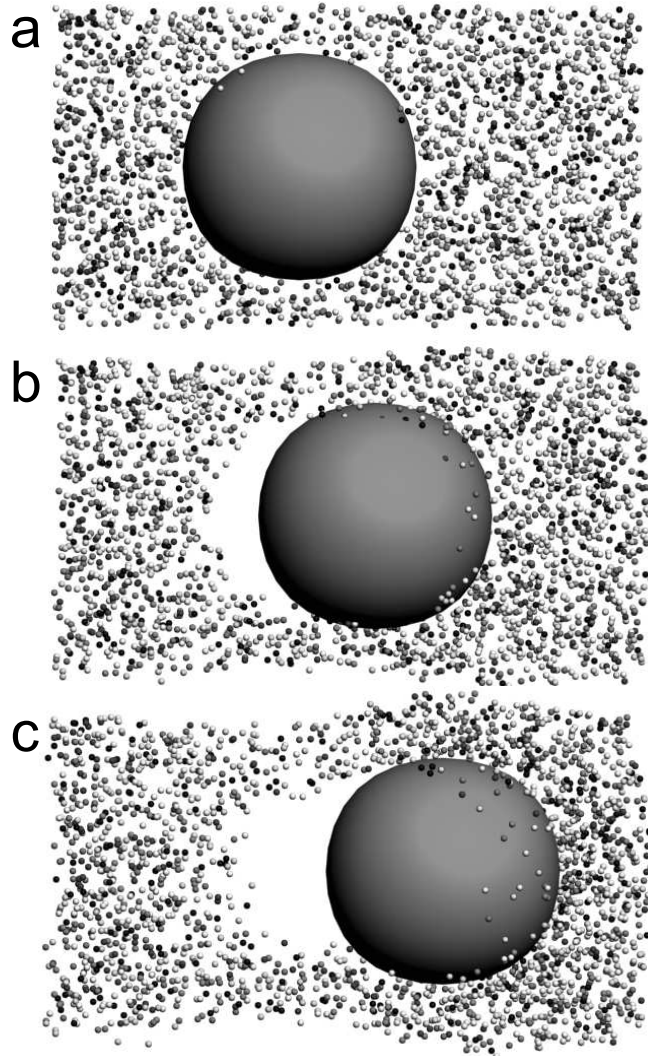


Figure 2.8: A series of snapshots of the bead moving under an applied constant external force as simulated by the DPD method. The applied force is directed to the right at time  $t_a$  (upper figure). The figures b and c are taken at times  $t_c > t_b > t_a$ . Note, that only a small amount of the monomers belonging to the polymers in the vicinity of the bead is shown. At the moment of application of the external force (a) the distribution of polymers around the bead is homogeneous. At times  $t_b$  and  $t_c$  the concentration of polymers in front of the bead is increased and behind is strongly decreased with respect to the concentration far from the bead.

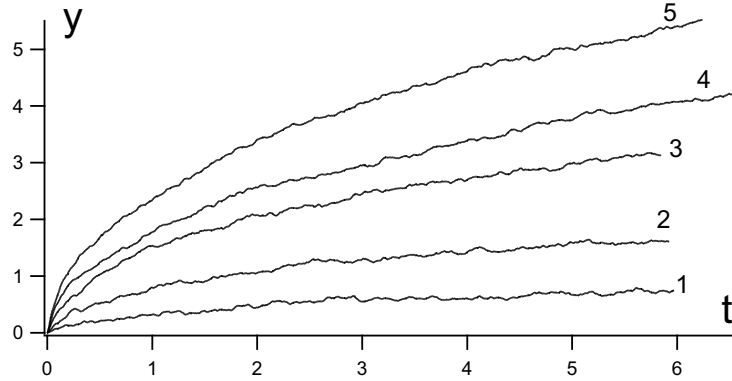


Figure 2.9: Typical response of the bead. Different responses correspond to different applied external forces:  $f_1 = 200$ ,  $f_2 = 400$ ,  $f_3 = 800$ ,  $f_4 = 1000$ ,  $f_5 = 1300$ . The force is applied at  $t = 0$ .

Typical responses of the bead on the applied constant external forces are shown in the Fig. 2.9. The number of polymers in these simulations is 4500 and the mesh size  $\xi$  of the entangled solution can be estimated using the following arguments. Divide the total volume of the system  $V$  in  $n$  cubes with the size  $\xi$ . Thus,  $n\xi^3 = V$ . The number  $n$  can be obtained as the ratio of the total lengths of all the polymers in the system  $\rho V$ , where  $\rho$  is defined by the Eq. 1.6, to the length of the edges of the small cubes per cube  $3\xi$ :  $n = \rho V / 3\xi$ . Combining these two equations we obtain

$$\xi = \sqrt{\frac{3V}{L \cdot N}}, \quad (2.13)$$

where  $V = L_x \cdot L_y \cdot L_z$ ,  $N$  is the number of polymers in the system and  $L$  is their contour length. Taking the dimensions of the simulation box 2.5, the contour length  $L = 34.5$  and the number of polymers  $N = 4500$ , we obtain  $\xi = 1.57$ . Therefore, the mesh size is approximately 12 times smaller than the diameter of the bead.

The same graph in a log-log scale is shown in the Fig. 2.10. The log-log representation clearly indicates the existence of different regimes of the motion of the bead. At early times,  $t \lesssim 0.2$ , the bead moves according to the power law  $y \sim t^\alpha$ , where  $\alpha \approx 0.75$  (the dashed line in the Fig. 2.10 has a slope 0.75). At times  $t \gtrsim 0.2$  the exponent of the power law changes to  $\alpha \approx 0.5$  (the dotted line in the Fig. 2.10 has a slope 0.5). This regime covers 2 decades in time.

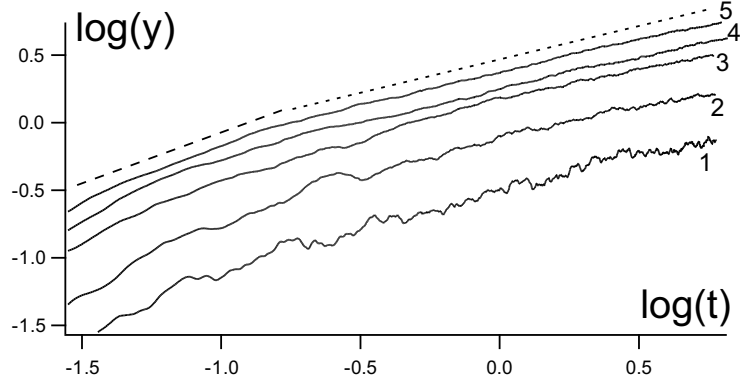


Figure 2.10: Responses of the bead to the applied force in the double logarithmic scale. Different responses correspond to different applied external forces:  $f_1 = 200$ ,  $f_2 = 400$ ,  $f_3 = 800$ ,  $f_4 = 1000$ ,  $f_5 = 1300$ . The mesh size in these simulations is  $\xi \approx 1.57$  units. The eye-guiding dotted line has a slope 0.5, and the dashed line 0.75.

### 2.5.3 Distribution of polymers around the moving bead

During the simulations the numbers of monomers neighboring the front and the rear hemispheres of the bead were separately stored. When no force is applied, these numbers are (approximately) equal, which is a consequence of the initial homogeneous distribution of polymers. As soon as the force is applied the number of neighbors in front of the bead grows while behind the bead it decreases. Both neighbor numbers saturate and remain approximately constant during the rest of the simulation. This is shown in the Fig. 2.11. It indicates that the polymer concentration in the close vicinity of the bead reaches steady distribution and stays constant during the enforced motion of the bead. This distribution is characterized by the increased polymer concentration in front of the bead and decreased behind with respect to the bulk polymer concentration.

The distribution of the polymer concentration around the bead was as well monitored during the simulations. Owing to the presence of the cylindrical symmetry in the problem we introduce a spherical coordinate system as shown in the Fig. 2.12. The origin of the coordinate system is the center of the bead and the azimuthal angle  $\theta$  is calculated with respect to the direction of the application of the external force. The polymer density  $c(r, \theta)$  is calculated as follows. Firstly, the numbers of monomers are counted in every cell of the two-dimensional grid, which is comprised by dividing the interval  $\theta \in [0, \pi]$  into 12 parts ( $\pi/12$  each) and the interval  $r \in [0, 20]$  into 20 parts. Secondly, to obtain the polymer concentration  $c(r, \theta)$  these numbers

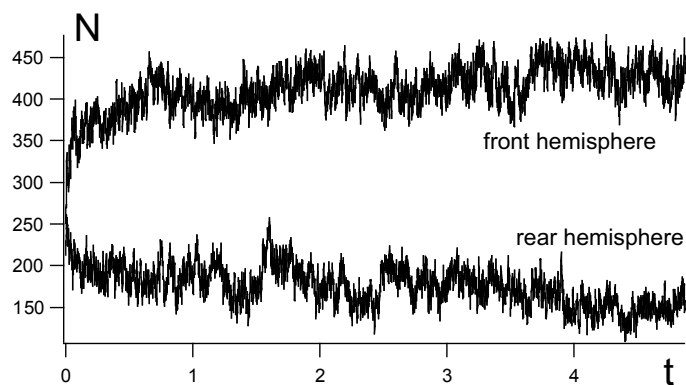


Figure 2.11: Number of monomers neighboring the bead at the front and at the rear hemispheres (indicated) as a function of time. The external force is applied at  $t = 0$ .

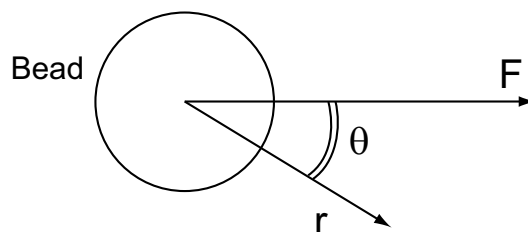


Figure 2.12: Orientation of the spherical coordinate system for the determination of the polymer concentration around the moving bead. The origin is in the center of the bead and the azimuthal angle  $\theta$  is calculated with respect to direction of the application of the force  $F$ .

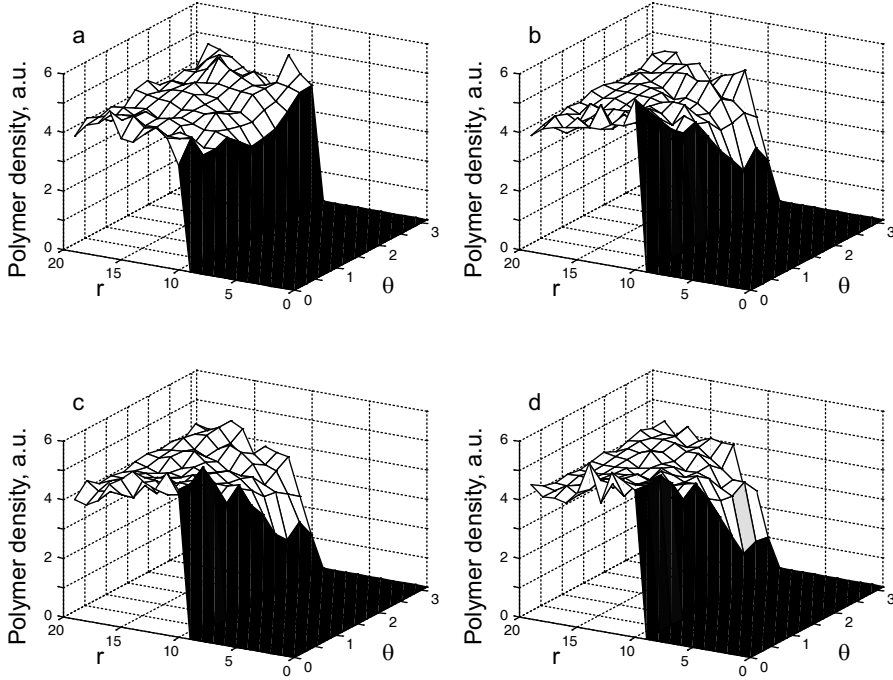


Figure 2.13: Polymer density as a function of the distance from the bead center  $r$  and the azimuthal angle  $\theta$ . The radius of the bead is 10. The graphs a, b, c, and d are the polymer densities at different times of the same simulation  $t_a = 0, 0 < t_b < t_c < t_d$ . The external force  $f = 1300$  is applied at  $t = t_a$ . Shown are the graphs corresponding to the mesh size of the polymer network  $\xi \approx 1.57$ .

are divided by the elementary volume  $r^2 \sin \theta$ .

A sequence of the polymer density distributions  $c(r, \theta)$  is shown in the Fig. 2.13. The graphs Figs. 2.13a, b, c, and d are the polymer densities at different points of time of the same simulation. The mesh size in this simulation is  $\xi \approx 1.57$  and the external force  $f = 1300$ . When no force is applied on the bead, i.e.  $t = 0$ , Fig. 2.13a, the distribution of polymers around the bead is uniform. As the bead moves due to the application of the external force the polymer concentration in front of the bead grows and decreases behind the bead, Figs. 2.13b, c, and d. This difference is clearly seen in the Fig. 2.14 where the polymer concentration profile in the vicinity of the bead  $c(r = R_b, \theta)$  is shown. This profile corresponds to the Fig. 2.13d.

The polymer concentration profiles in the vicinity of the bead in simulations with the mesh size  $\xi \approx 1.57$  with the external forces taking the values  $f = 200, 400, 800, 1000$  and  $1300$  are shown in the Fig. 2.15. Clearly seen is the increase in the concentration difference in front and behind the bead

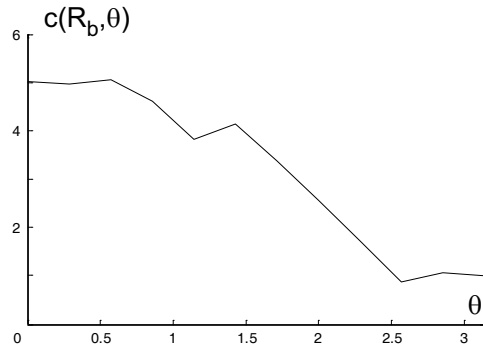


Figure 2.14: Polymer concentration profile in the vicinity of the bead ( $r = R_b$ ) at time  $t_d$  of the simulation from the Fig. 2.13 as the function of the azimuthal angle  $\theta$ .

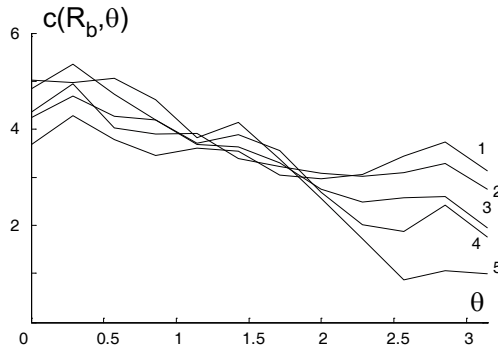


Figure 2.15: Polymer concentration profiles in the vicinity of the bead ( $r = R_b$ ) in the square root regime of the bead motion as the function of the azimuthal angle  $\theta$ . Shown are the graphs corresponding to the mesh size  $\xi \approx 1.57$ . The curves correspond to different forces  $f_1 = 200$ ,  $f_2 = 400$ ,  $f_3 = 800$ ,  $f_4 = 1000$  and  $f_5 = 1300$  force units.

with increasing external force. The consequence of this polymer concentration difference is the additional force, which will be shown to be osmotic in origin, resisting the motion of the bead.

### 2.5.4 Forces resisting the moving bead

As it has been shown, the enforced motion of a microbead in a solution of semiflexible polymers exhibits a square root dependence of its position on time within several time decades, see Figs. 2.9 and 2.10. This regime is characterized by the increased concentration of polymers in front of the bead while it is strongly decreased behind the bead, Fig. 2.14. Therefore, besides the viscous force acting on the moving bead due to the viscosity of the fluid, the polymers exert an additional force, which as well resists the bead motion.

Computer experiments permit direct monitoring of the forces exerted on the bead by the water and monomer spheres separately. Let  $F_v$  denote the projection of the total force exerted on the bead by the neighboring water spheres on the direction of the bead motion.  $F_v$  consists of the conservative, random and viscous contributions, eq. 2.2. We interpret it as the viscous force experienced by the bead.

Let  $F_{\text{pol}}$  denote the force which is defined similar to  $F_v$  except that it is the projection of the total force exerted by the neighboring polymers. These forces as the functions of time obtained during the simulation of the enforced motion of the bead are depicted in the Fig. 2.16. The external force applied on the bead in this simulation is 1000 force units and the mesh size is  $\xi \approx 1.57$ . It can be seen, Fig. 2.16a, that the force  $F_{\text{pol}}$  is approximately zero at the moment of the application of the external force, which is a consequence of the initial uniform distribution of the polymers around the bead. At later times as the bead moves and the polymer concentration in front of the bead becomes higher than that behind the bead, the resisting force due to polymers gradually grows. The force  $F_{\text{pol}}$  grows with the increasing concentration of polymers at the front hemisphere of the bead and rapidly becomes on average equal to the external force. In contrast, the viscous force experienced by the bead, Fig. 2.16b, in the very beginning of its motion is close to the external force, Fig. 2.16c. Later, as the velocity of the bead decreases this force becomes much smaller than the resistance force due to polymers.

### Contributions to the polymer resistance force

The resistance force created by the neighboring monomers  $F_{\text{pol}}$  consists of the conservative contribution  $F_{\text{pol}}^c$ , the random contribution  $F_{\text{pol}}^r$  and the viscous contribution  $F_{\text{pol}}^v$ , Eq. 2.2. As seen in the Fig. 2.17 the viscous contribution

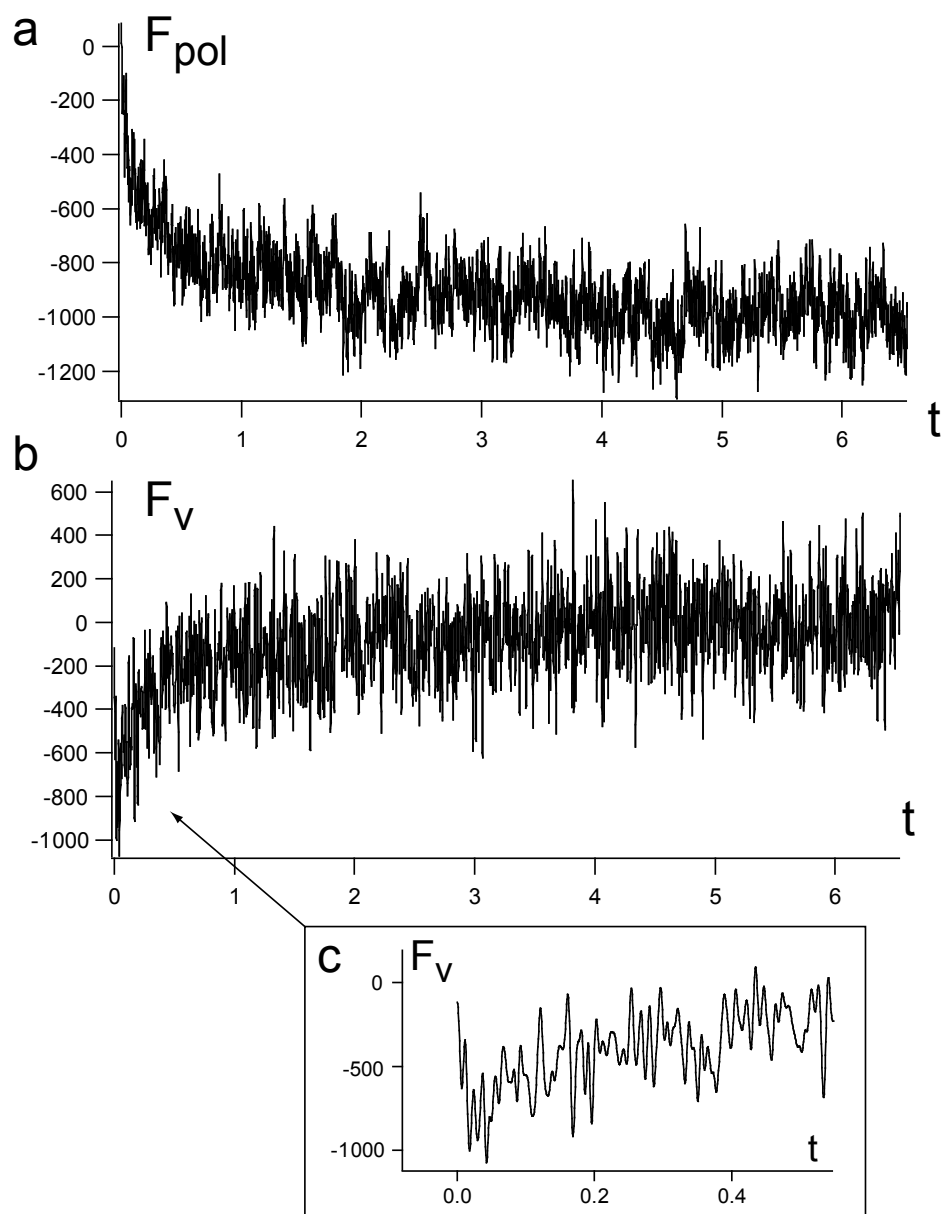


Figure 2.16: The forces exerted by the polymers  $F_{\text{pol}}$  (a) and by the fluid  $F_v$  (b, c) acting on the moving bead. The external force applied on the bead is 1000, the mesh size  $\xi \approx 1.57$ .

$F_{\text{pol}}^{\text{v}}$  is more than 4 orders of magnitude smaller than the sum  $F_{\text{pol}}^{\text{c}} + F_{\text{pol}}^{\text{r}}$ , which can be interpreted as the osmotic force exerted by the polymers on the bead. The conservative force Eq. 2.3 represents a steric repulsion. Therefore, the main contribution to the resisting force  $F_{\text{pol}}^{\text{c}}$  originates from the pressure, which the polymers piled up in front of the bead exert on its surface. The pressure arises from the local entropy decrease and is thus related to the osmotic pressure. Therefore, the resistance force  $F_{\text{pol}}$  is mainly osmotic in origin and can be denoted as  $F_{\text{osm}}$ .

Thus, at the initial stage of the motion of the bead, when the distribution of polymers around the bead is still approximately uniform, the motion of the bead is dominated by the viscosity of the water. The osmotic force in this regime is small compared to the viscous force exerted by water on the bead. It is followed by the regime in which the compliance of the bead experiences the square root dependence on time. **In this regime the motion of the bead is dominated by the osmotic force.** On average the osmotic force due to the polymer concentration difference in front of and behind the bead is at this stage close to the externally applied force.

The time dependencies of the ratio of the force exerted by polymers to the external force  $f$  are similar to each other for all simulations as shown in the Fig. 2.18. The value  $F_{\text{osm}}/f$  quickly approaches -1 indicating that the osmotic force provides the main contribution to the resistance force experienced by the bead.

### 2.5.5 Microrheology of solutions with various concentrations of polymers

We performed simulations of the enforced bead motion in polymer solutions with various polymer concentrations. The responses of the bead in the polymer solutions with the mesh sizes  $\xi \approx 1.67$ ,  $\xi \approx 1.78$ , and  $\xi \approx 1.96$  are shown in the Figs. 2.19a, b, and c, respectively. The same data in the log-log scale is depicted in the Fig. 2.20. For every polymer concentration simulations with 5 different external forces of 200, 400, 800, 1000, and 1300 force units have been done.

Analogously to the case shown in the Fig. 2.10 where the mesh size of the network was  $\xi \approx 1.57$  units, one can distinguish the initial regime when the dependence of the bead displacement on time exhibits a power law  $y \sim t^\alpha$  with  $\alpha \approx 0.75$ . This regime is indicated in the Fig. 2.20 by the lines with the slope 0.75 and takes place at times  $t \lesssim 0.2$ .

At times  $t \gtrsim 0.2$  the displacement of the bead is described by the power law  $y \sim t^\alpha$  with  $\alpha$  close to 0.5. The slopes of the responses, which give the

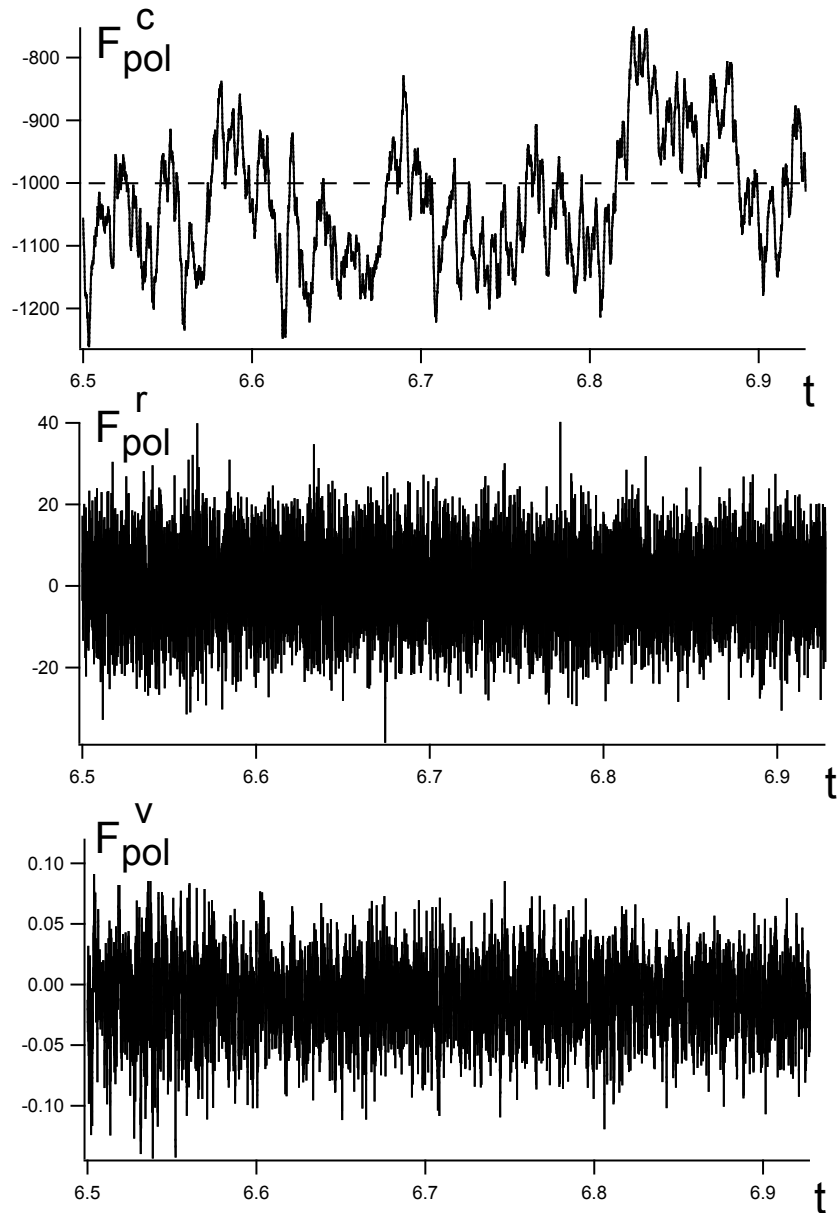


Figure 2.17: The conservative  $F_{\text{pol}}^c$ , the random  $F_{\text{pol}}^r$  and the viscous  $F_{\text{pol}}^v$  contributions to the polymer resistance force  $F_{\text{pol}}$  experienced by the bead in active microrheological experiments. The data corresponds to the Fig. 2.16 and the dashed line in the upper graph indicates the value  $-f$ .

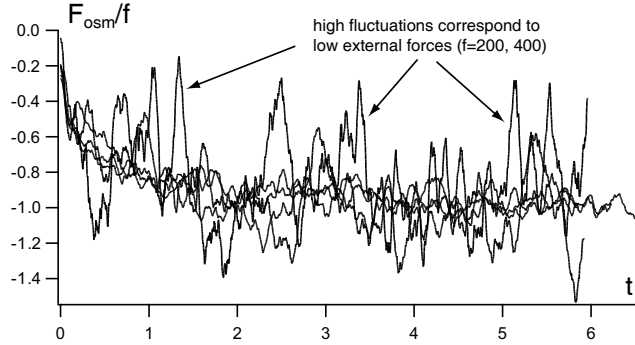


Figure 2.18: The ratios of the force exerted by polymers to the external force on the bead  $f$  as functions of time for a set of 5 simulations with the mesh size  $\xi \approx 1.57$ . The external forces take the values 200, 400, 800, 1000, and 1300. All dependencies fall approximately on the same curve. The lower the external force is, the higher the fluctuations are. The curves on this graph had been smoothed compared to the ones in the Fig. 2.16.

exponents, are indicated in the Fig. 2.20.

In order to reveal the influence of the polymer concentration on the enforced bead motion the responses of the bead have been fitted by the expression  $y = A\sqrt{t}$ . The dependence of the coefficient of the square root regime  $A$  on the polymer contour length density  $\rho$ , Eq. 1.6,  $A(\rho)$  in the log-log scale is shown in the Fig. 2.21. For relatively high forces the dependence is close to a power law  $A \sim \rho^{-1.4}$ .

### 2.5.6 Responses of the bead to various force amplitudes

In order to check the dependence of  $A$  on the external force  $f$  applied on the bead, various simulations have been performed at different polymer concentrations and the external forces taking values 200, 400, 800, 1000 and 1300. The resulting dependencies  $A(f)$  in log-log scales are shown in the Fig. 2.22. The linear fits for all four concentrations yield slopes close to 1. Therefore,  $A \sim f^\alpha$ , where  $\alpha \approx 1$ . Thus, our DPD approach fails to reproduce the  $A \sim f^{0.75}$  scaling found in the recent experiments described in the Sec 1.3.3. This failure can be due to the periodic boundary conditions, which have to be employed in the simulations, as well as it can be due to the insufficiently large simulation box. Another plausible reason may be related to an additional interaction between the actin polymers present in the experiments such as a weak cross-linking, which is not accounted for in the simulation method.

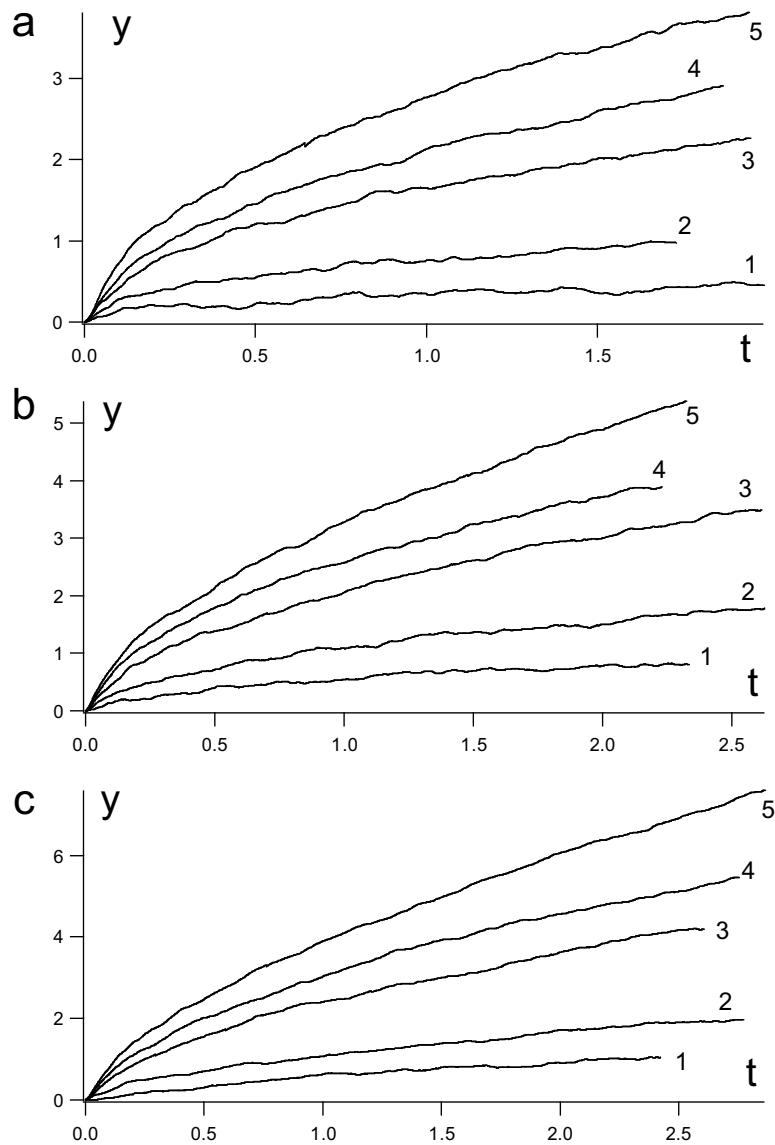


Figure 2.19: Responses of the bead to the constant external force in solutions with various concentrations of polymers. In all graphs the curves indicated by the numbers from 1 to 5 correspond to external forces 200, 400, 800, 1000, and 1300, respectively. The responses of the graph (a) are taken in the polymer solution with the mesh size  $\xi \approx 1.67$ , whereas that in the graph (b) is  $\xi \approx 1.78$ , and in the graph (c)  $\xi \approx 1.96$ .

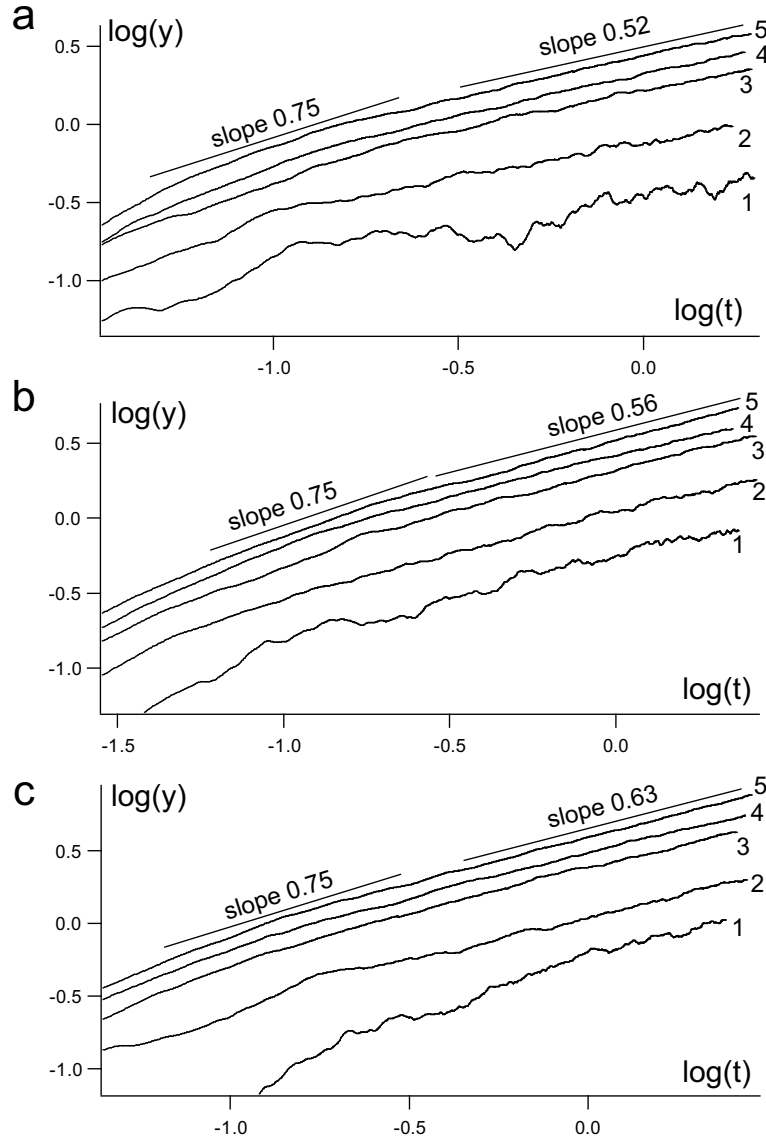


Figure 2.20: Responses of the bead in solutions with various polymer length densities, Fig. 2.19, in the log-log scale. In all graphs curves 1, 2, 3, 4, and 5 correspond to external forces 200, 400, 800, 1000, and 1300, respectively. The responses of the graph (a) are taken in the polymer solution with the mesh size  $\xi \approx 1.67$ , whereas that in the graph (b) is  $\xi \approx 1.78$ , and in the graph (c)  $\xi \approx 1.96$ . The slopes indicate the two regimes of the bead motion. At the early stage the response slope is close to 0.75, while at the later stage the slope varies from 0.52 (a) to 0.63 (c).

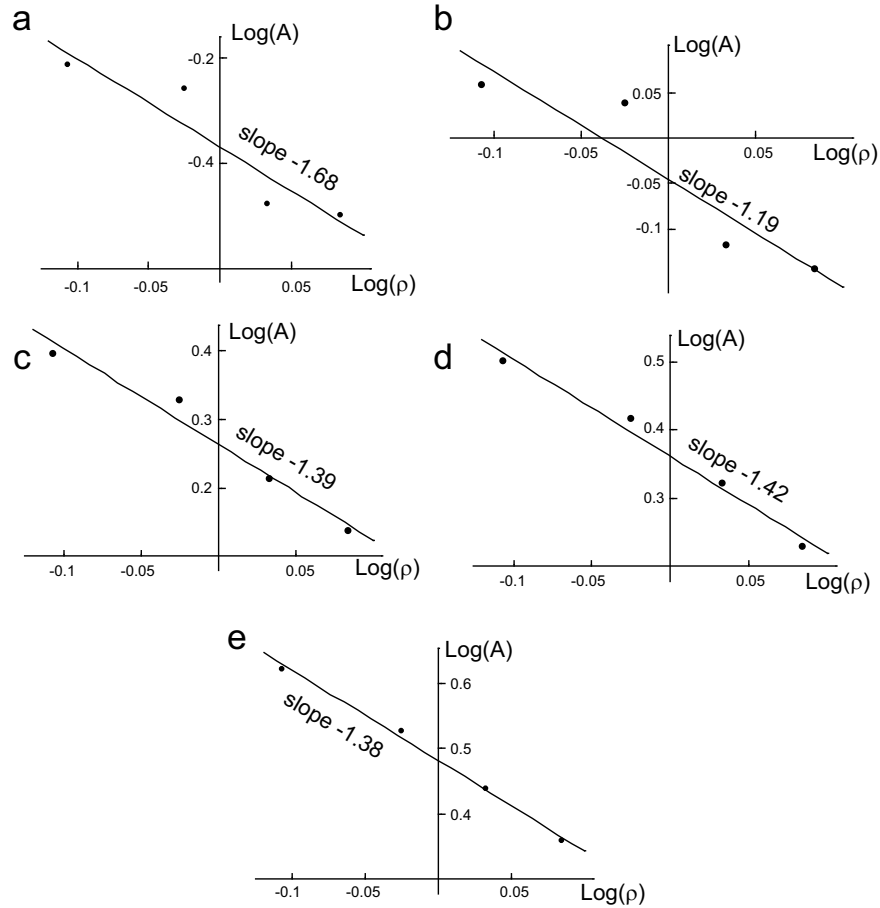


Figure 2.21: Dependence of coefficient of the square root regime  $A$ , obtained by fitting the responses of the bead on the constant external force by the expression  $y = A\sqrt{t}$ , on the polymer contour length density  $\rho$ , Eq. 1.6 in the log-log scale. The graphs a, b, c, d, and e correspond to the external forces  $f = 200, 400, 800, 1000$ , and  $1300$ , respectively. The solid lines are linear fits.

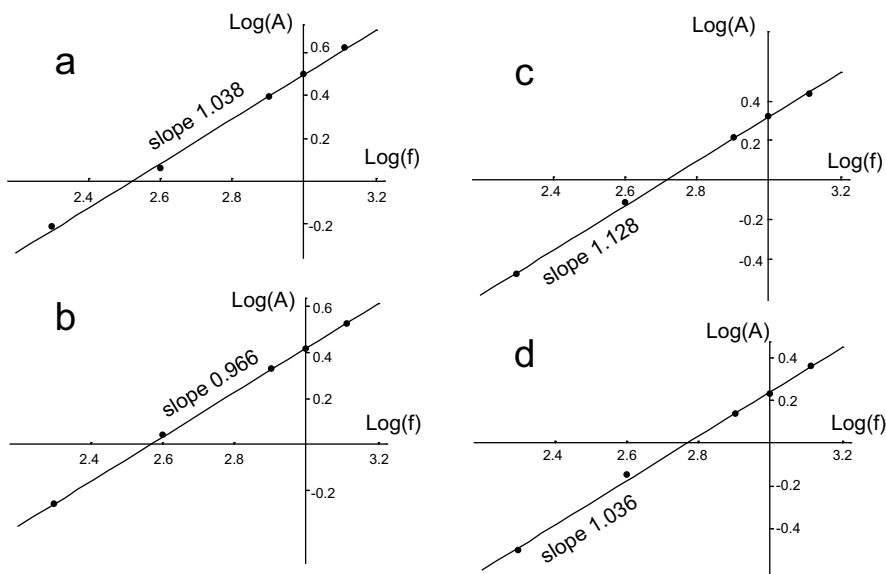


Figure 2.22: Dependencies of  $A$ , obtained by fitting the responses of the bead with the expression  $y = A\sqrt{t}$ , on the external force  $f$  applied on the bead. Graphs a, b, c, and d correspond to different concentrations of polymers with mesh sizes  $\xi \approx 1.96, 1.78, 1.67,$  and  $1.57$ , respectively. The solid lines are linear fits. Their slopes are close to 1 indicating a linear dependence of  $A$  on  $f$ .

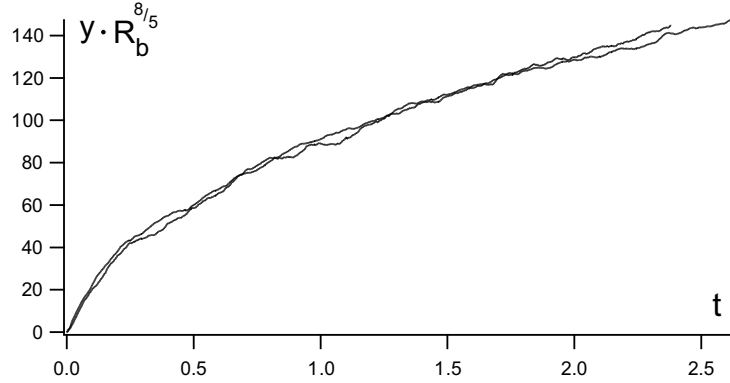


Figure 2.23: Responses of the beads with radii  $R_b = 10$  and  $R_b = 13$  multiplied by  $R_b^{8/5}$  on the constant external force.

### 2.5.7 Beads of different sizes

A larger simulation box would offer a possibility to perform the simulations of microrheology with different sizes of the probing bead. For this reason we have made two simulations with a larger simulation box with the dimensions  $L_x = 60$ ,  $L_y = 80$  and  $L_z = 60$ . The mesh size in these simulations was  $\xi \approx 1.57$  and the external force applied on the bead  $f = 1000$ . Two simulations in such a box have been carried out with the radii of the bead  $R_b = 10$  and  $R_b = 13$ . The responses of the bead multiplied by  $R_b^{8/5}$  are shown in the Fig. 2.23.

### 2.5.8 Microrheology of solutions of polymers possessing various diffusion coefficients

Computer simulations provide a much greater flexibility and open broader opportunities with respect to conventional experiments in changing the parameters of the system under study as well as in measuring required quantities in the studied system. By changing the dissipative force constant  $\gamma_{mw}$  of monomer-water interaction one can alter the longitudinal diffusion coefficient  $D_{\parallel}$  of the simulated semiflexible polymers as shown in the Sec. 3.3. Consequently, without altering the viscosity of the solvent or the contour length of the polymers one can control their diffusion coefficient.

Three additional simulations of active microrheology of polymer solutions with the mesh size  $\xi \approx 1.57$  have been performed with different dissipative force constants lower than the one used previously  $\gamma_{mw} = 1$ . The values of the dissipative force constants were taken to be  $\gamma_{mw} = 0.2, 0.4$  and  $0.7$ . Lower value of the dissipative force constant leads to higher longitudinal diffusion

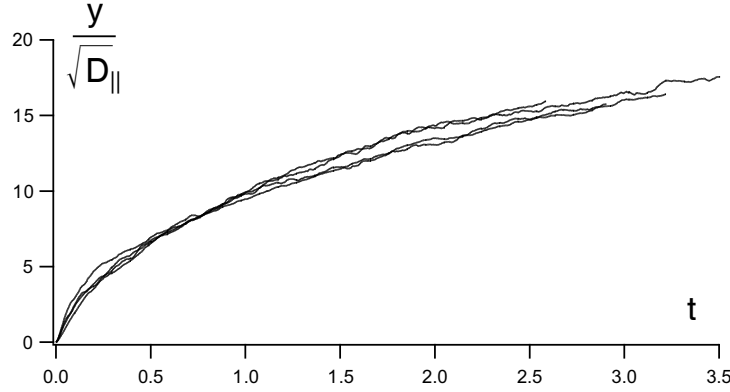


Figure 2.24: Four responses of the bead normalized by  $\sqrt{D_{\parallel}}$  in simulations with different dissipative force constants  $\gamma_{\text{mw}}$  of monomer-water interaction. The longitudinal diffusion coefficients of polymers are determined in the Sec. 3.3.

coefficients  $D_{\parallel}$  as shown in the Sec. 3.3. The measured diffusion coefficients are summarized in the Tab. 3.3 on the page 60. Therefore, we have four different simulations of the enforced bead motion taken with the external force of 1000 force units.

The responses of the bead normalized by  $\sqrt{D_{\parallel}}$  are shown in the Fig. 2.24. The responses fall on the same curve suggesting that

$$y \sim \sqrt{D_{\parallel}}, \quad (2.14)$$

## 2.6 Conclusions

This chapter has been concerned with the simulations of the active microrheology of semiflexible polymer solutions. The responses of the bead in such solutions on external forces have been studied.

The responses clearly show the presence of two different regimes of the bead motion. In the initial regime the response of the bead exhibits a power law  $y \sim t^{0.75}$ . At the subsequent stage the displacement of the bead is given by  $y \approx At^{\alpha}$  with  $\alpha \approx 0.5$ . We have found the linear dependence of the response on the applied force,  $A \sim f$ , the square root dependence on the longitudinal diffusion coefficient  $A \sim \sqrt{D_{\parallel}}$  and the power law dependence on the polymer concentration  $A \sim c^{-\gamma}$  with  $\gamma \approx 1.4$ .

We established that the polymers are piled up in front of the bead, while behind the bead the fluid is (almost) free of polymers. We analyzed the force resisting the motion of the bead and established that in the square root regime the motion is governed by the osmotic force.

Another open question, which should be addressed, is the character of the motion of polymers around the moving bead. Knowing the character of the polymer motion in active microrheological experiments may help building an analytical model. Therefore, in the next chapter we study the motion of semiflexible polymers in solutions in order to compare with that in the active microrheological experiments.

# Chapter 3

## Diffusion of semiflexible polymers in solutions

Diffusional properties of semiflexible polymers in solutions are important for their viscoelastic properties. Such quantities as the relaxation time of the modes with wavelengths shorter than  $L_e$ , which determines the time window of the high frequency viscoelastic response, or the reptation time, which is a typical time scale of the polymer density fluctuation relaxation, are directly connected to the diffusion of polymers. Whereas the former is related to a free diffusion of the polymers, the latter is greatly influenced by the steric constraints present in polymer solutions. In other words, it is a matter of time scales: on the time scale shorter than the entanglement time the polymers do not feel the surrounding network, whereas on the longer time scales collective effects come into play.

It is generally assumed [31] that the friction coefficients, which yield the frictional force per unit length and per unit velocity of the polymer, can be estimated as

$$\zeta_{\parallel} \simeq 2\pi\eta/\ln(\xi_{\parallel}/d), \quad \zeta_{\perp} \simeq 4\pi\eta/\ln(\xi_{\perp}/d), \quad (3.1)$$

where  $\zeta_{\parallel}$  and  $\zeta_{\perp}$  are respectively the friction coefficients for the motion of the polymer parallel and perpendicular to the polymer backbone,  $\eta$  is the solvent viscosity,  $\xi_{\parallel}$  and  $\xi_{\perp}$  are the hydrodynamic screening lengths describing the distance to which the fluid velocity field created by a moving polymer penetrates away from the polymer backbone, and  $d$  is the polymer backbone diameter.

In order to characterize the diffusional properties of semiflexible polymers in solutions and elucidate the effect of the polymer concentration and polymer contour length additional simulations have been performed. In contrast to the active microrheological studies, Sec. 2.5, we simulated polymer solutions

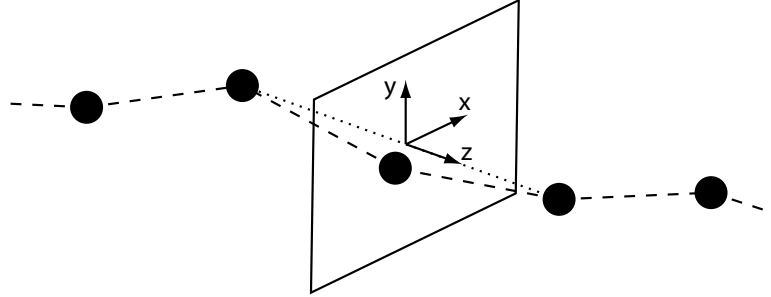


Figure 3.1: A plane of cross-section with the coordinate system. Note, that the lengths of the bonds are exaggerated.

without microbeads. The size of the simulation box has been set to 40 in all directions. As in the microrheological studies, Sec. 2.5, we used periodic boundary conditions, except for the non-slip boundary layers, which were released. The following procedure has been used to study the transversal and longitudinal diffusion coefficients of semiflexible polymers.

In the initial moment of time of each simulation  $N$  cross-sectioning planes were introduced for every polymer as shown in the Fig. 3.1. The points of cross-sections are chosen to be every 10th monomer of a polymer, i.e. a 70 monomer long polymer is initially cross-sectioned at monomers 9, 19, 29, 39, 49, and 59, which gives, therefore,  $N = 6$  cross-section planes per polymer. The cross-section planes are initially defined as to be normal to the lines connecting two neighboring monomers, Fig. 3.1, and a coordinate system is assigned to every plane with  $z$ -axis being normal to the respective plane. Total number of cross-sections for each simulation is of the order of 10000 providing a rich statistics.

During the simulation the  $(x, y)$  coordinates of the points of intersections of polymers with the cross-section planes were stored as well as the  $z$  coordinates of the monomers, which initially defined the positions of the sectioning planes. While the latter were interpreted as the longitudinal displacements of polymers, the former were assigned to be the transversal displacements.

The simulations result in the sets of transversal and longitudinal displacements of polymers for every cross-section, which are analyzed in the following way. The transversal displacements of the polymers form clouds of points for every cross-section, Fig. 3.2, which are not necessarily centered around zero. This is due to the fact that at the beginning, as the coordinate systems in the cross-section planes are defined, the polymers are not necessarily situated along the centerlines of their tubes. Therefore, in order to find the average radius of the clouds of transversal displacements of polymers at time  $t$  of

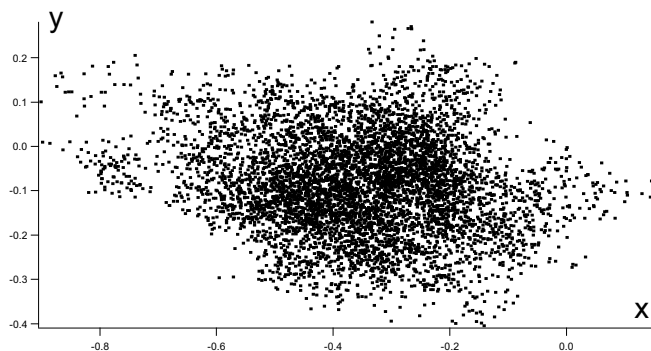


Figure 3.2: A typical cloud of transversal displacements of a polymer during the simulation.

the simulation the centers of the clouds for all cross-sections formed by the transversal displacements of the polymers within the time interval  $[0, t]$  were found. After that all the clouds were combined into one and a histogram of displacements with respect to the distance to the origin was formed. The histogram was then fitted by a gaussian distribution

$$C \exp\left(-\frac{r^2}{2R_{\perp}^2}\right), \quad (3.2)$$

where  $r$  is the distance to the center of the joint cloud,  $R_{\perp}$  is the fitting parameter, and  $C$  is the normalization constant. The fitting procedure, therefore, gives the dependence  $R_{\perp}(t)$  of the radius of the cloud on time.

A similar procedure is used for the study of longitudinal diffusion except that no center of cloud determination is needed because the joint cloud is already centered around zero due to the fact that the monomers, the distances to which from the cross-section planes are tracked during the simulations, are initially located in the cross-section planes. Therefore, the procedure gives the dependence  $R_{\parallel}(t)$ . We compare the obtained dependencies with the case of a one-dimensional diffusion of a free particle for which the mean square displacement is given by

$$\langle R^2(t) \rangle = 2Dt, \quad (3.3)$$

where  $D$  is the diffusion coefficient.

### 3.1 Short time diffusion of semiflexible polymers

A number of simulations has been performed with various polymer concentrations and contour lengths in order to analyze the influence of these quantities

on the diffusional properties of the semiflexible polymers. For convenience the simulations were carried out with the cubic simulation box with dimensions  $L_x = 40$ ,  $L_y = 40$  and  $L_z = 40$ . The simulations can be divided into two sets. The first one is a set of simulations with the constant polymer contour length of 34.5 units (70 monomers in a polymer) with various numbers of polymers yielding the mesh sizes of the network according to the Eq. 2.13 represented in the Tab. 3.1.

Table 3.1: Mesh sizes of the simulated polymer networks in a set of simulations with constant polymer contour length of 34.5 units.

Simulation	1	2	3	4	5	6	7	8
Number of polymers	2500	2250	2125	2000	1875	1750	1625	1500
Mesh size, $\xi$ (length units)	1.49	1.57	1.62	1.69	1.72	1.78	1.85	1.93

The simulations of the second set are performed at a constant mesh size of  $\xi \approx 1.57$  and with the polymer contour lengths taking the values represented in the Tab. 3.2. The polymer contour length in some simulations exceeds, therefore, the dimensions of the cubic simulation box with the size of 40 units, which may cause the spurious self-interaction of polymers due to the periodic boundary conditions. The number of spuriously interacting polymers in a system with the contour length of the polymers of 79.5 is less than 2% of the total number of polymers and it is even smaller in the systems with shorter polymers. Consequently, this spurious interaction should not influence the statistics, which is obtained by averaging over all polymers in the system.

Table 3.2: Polymer contour lengths in the set of simulations at constant mesh size  $\xi \approx 1.57$ .

Simulation	1	2	3	4	5	6	7
Polymer contour length, $L$ (length units)	24.5	34.5	44.5	52	59.5	69.5	79.5

The short time diffusion of a polymer in solutions is defined as the diffusion within the characteristic time  $\tau_e$  between successive collisions of the polymer with its tube. It can be regarded as diffusion of a free polymer.

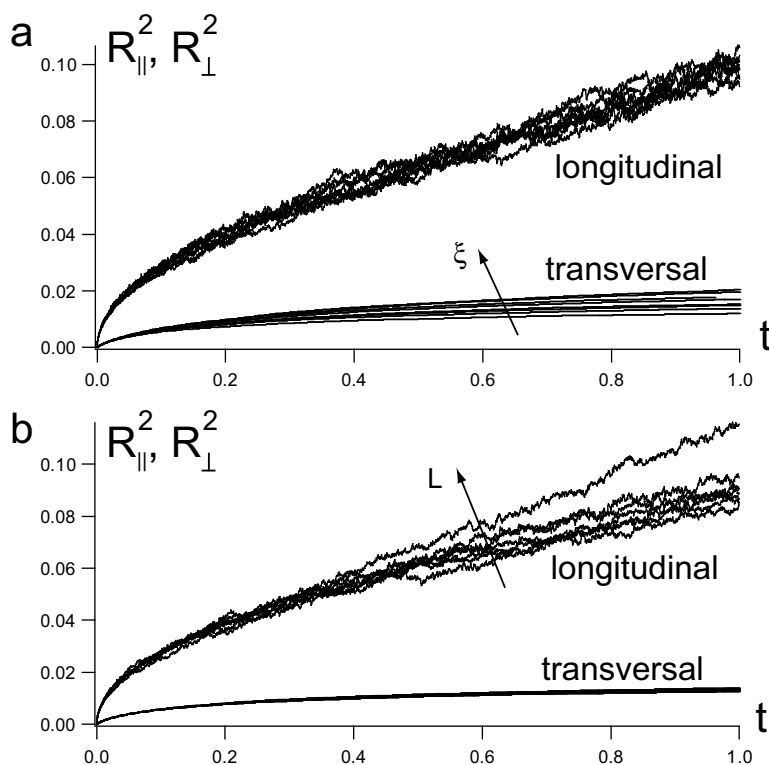


Figure 3.3: Mean square longitudinal and transversal displacements of semiflexible polymers. (a) A set of simulations with various polymer concentrations (mesh sizes) and a constant contour length of the polymers, (b) A set of simulations at a constant concentration of polymers, but with various polymer contour lengths (see text). Arrows show the variations from curve to curve of the mesh size (a) and polymer contour length (b).

The longitudinal and transversal mean square displacements of polymers for the two sets of simulations in the time domain  $t \in [0, 1]$  are shown in the Figs. 3.3. The transversal polymer diffusion is, as seen from the Fig. 3.3a, is very much influenced by the concentration, i.e. the mesh size, of the polymer solution. In contrast, the contour length of the polymers at constant mesh size has no effect on the transversal diffusion – the transversal MSDs<sup>1</sup> of the Fig. 3.3b fall on the same curve. In turn, the mesh size has no apparent influence on the longitudinal diffusion of polymers, whereas there is a contour length dependence of the longitudinal MSD.

Nevertheless, the transversal and longitudinal mean square displacements of polymers at different concentrations and polymer contour lengths share

<sup>1</sup>MSD - mean square displacement

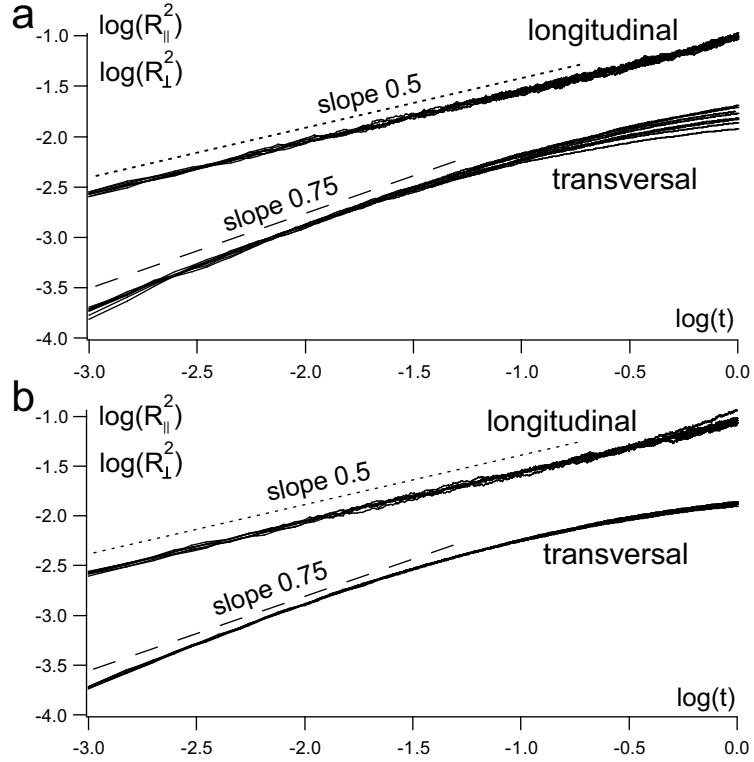


Figure 3.4: The data of the Figs. 3.3 in log-log scale. The dotted lines possess slopes 0.5 corresponding to the power law dependence of the MSDs  $t^{0.5}$ , while the dashed lines have slopes 0.75 and correspond to the power law  $t^{0.75}$ .

common features in the initial dependence on time shown in the Figs. 3.4. The initial regime of the transversal mean square displacement of polymers as it has been shown in [8, 60] is a power law  $R_{\perp}^2(t) \sim t^{\alpha}$  with the exponent  $\alpha = 0.75$ . This power law holds for times  $t < \tau_e$ , i.e. for times shorter than the characteristic collision time of the polymers with the surroundings. At longer times the transversal mean square displacement saturates reflecting the fact that after the polymer has explored its tube the following transversal motion is severely hindered by the steric constraints.

The longitudinal mean square displacement of semiflexible polymers shows a power law dependence on time at the initial stage of motion with the exponent 0.5, Figs. 3.4. This sub-Fickian diffusion has been observed in simulations and is a consequence of the extensibility of polymer chains [61].

## 3.2 Long time diffusion of semiflexible polymers

In this section we consider the long time diffusion of semiflexible polymers, which is characterized by a saturation in the transversal mean square displacement and a linear scaling of the longitudinal MSD with time. Mean square longitudinal displacements  $R_{\parallel}^2$  of polymers of constant contour length of 34.5 units at various mesh sizes from the Tab. 3.1 are shown in the Fig. 3.5a. We find no noticeable influence of the mesh size of the network on the longitudinal diffusion of polymers. In contrast, the transversal diffusion is influenced by the polymer concentration. The transversal MSDs  $R_{\perp}^2$  of polymers are shown in the Fig. 3.5b. It can be seen that the transversal MSD tends to saturate at different values depending on the mesh size of the network.

Results of the set of simulations of polymer networks with various polymer contour lengths at a constant mesh size  $\xi \approx 1.57$  are shown in the Fig. 3.6. The longitudinal MSD is strongly dependent on the contour length of the polymers as can be seen from the Fig. 3.6a. The curves in the Fig. 3.6a corresponding to different polymer contour lengths possess different slopes, which are determined by the longitudinal diffusion coefficients. At the same time, the Fig. 3.6b shows that there is no influence of the polymer contour length on the diffusional properties of polymers transverse their tubes.

The square root of the saturation value of the transversal MSD  $\sqrt{R_{\perp}^2}$  is directly related to the radius of the fluctuation tube  $R_e$ . Since the size of the monomers in the simulations is comparable with the saturation value of the transversal MSD, the average radius of the tube is given by  $R_e = R_m + R_{\perp}$ , where  $R_m$  is the radius of the monomers. In order to elucidate the effect of the concentration of polymers on the average tube radius  $R_e$  the values  $R_{\perp}$  are taken at the moment  $t = 5$  of the simulations and the tube radius is plotted against the mesh size  $\xi$  in the Fig. 3.7. The data are fitted with a line suggesting the linear scaling of the tube radius with the mesh size  $R_e \sim \xi$  in accordance with the Eq. 1.8, since from the Eq. 2.13 we get  $\xi \sim \rho^{-1/2}$ . The coefficient of proportionality between the average radius of the reptation tubes  $R_e$  and the mesh size  $\xi$ , which would be useful to obtain, can not be extracted from our simulations since in the simulations the monomer radius  $R_m$  is comparable with the mesh size whereas in real systems the polymer backbone diameter is about two orders of magnitude smaller than the mesh size.

The longitudinal diffusion coefficient of polymers can be extracted by fitting the linear part of the mean square longitudinal displacement  $R_{\parallel}^2$  of polymers as shown in the Fig. 3.6. The diffusion coefficients obtained in such

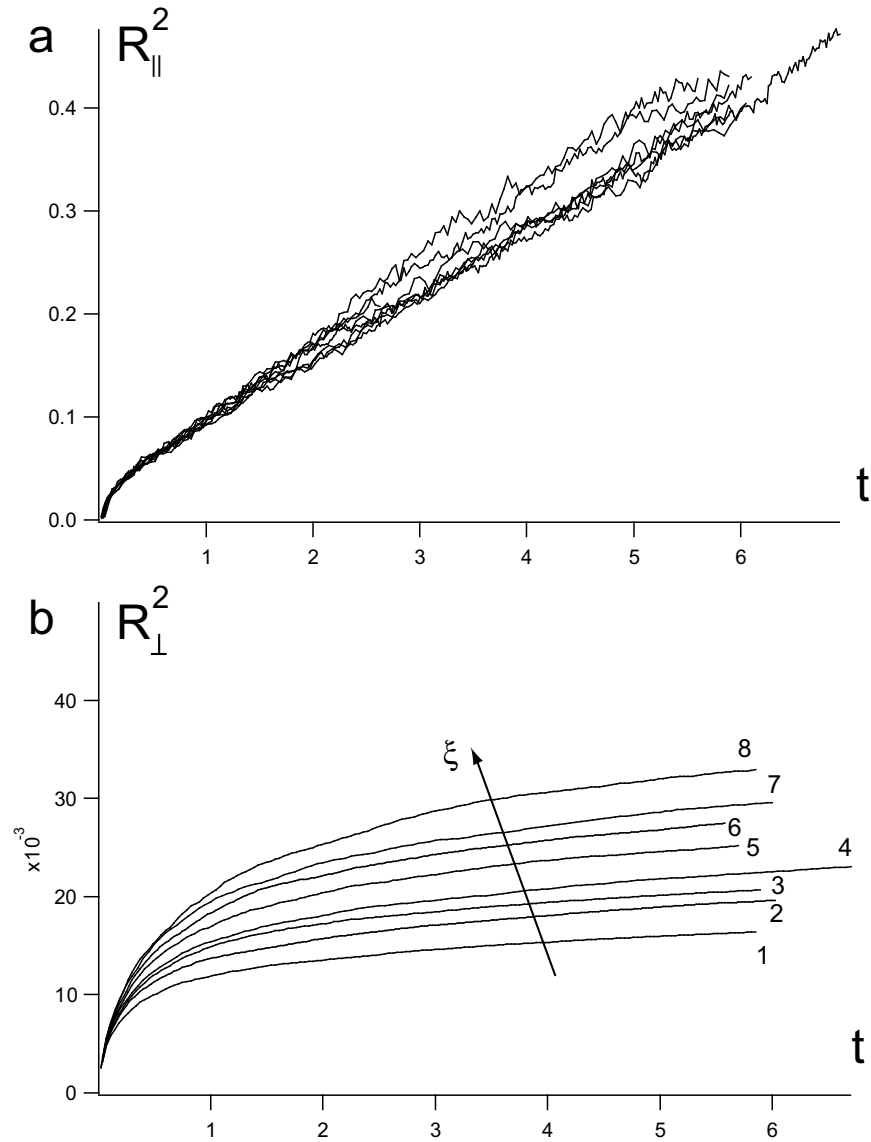


Figure 3.5: Longitudinal (a) and transversal (b) MSD of 34.5 units long polymers in polymer networks of various mesh sizes. The curves in the bottom figure are numbered according to the Tab. 3.1. Additional axis indicates the change in the mesh size  $\xi$  from simulation to simulation.

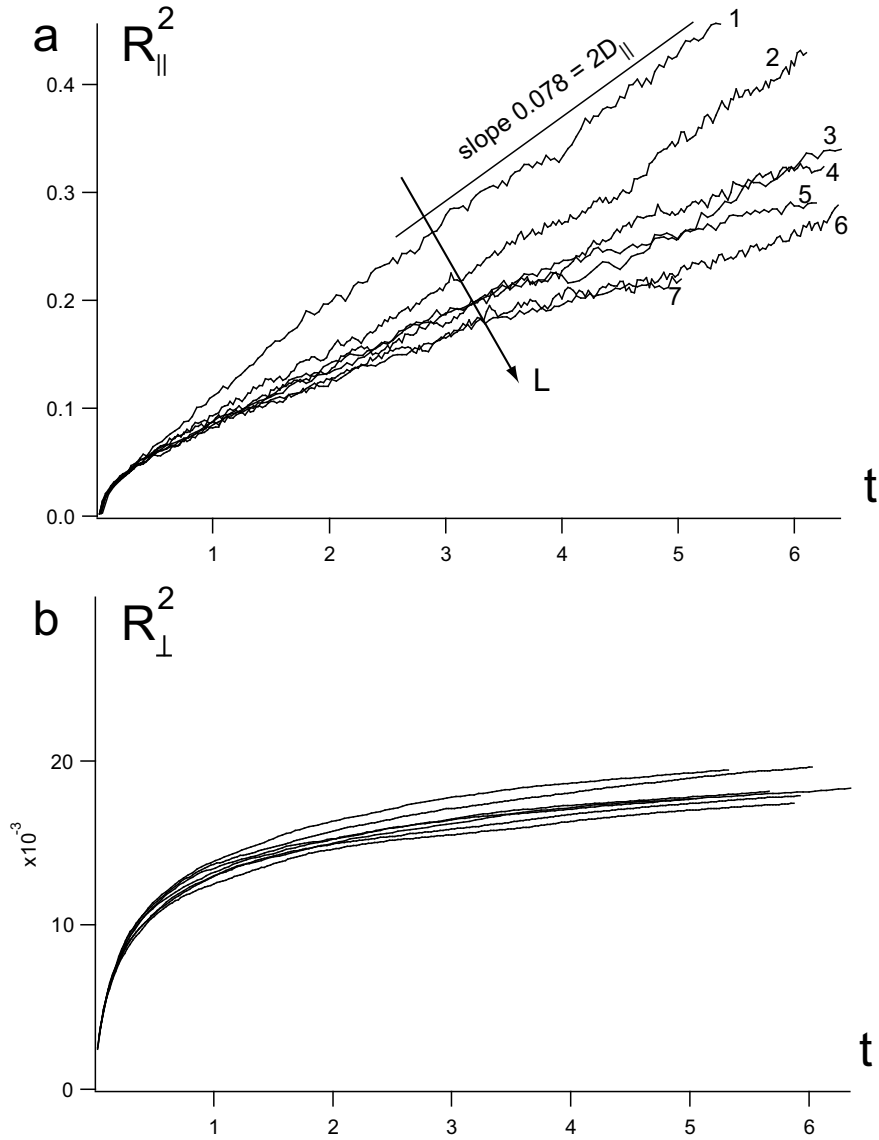


Figure 3.6: Longitudinal (a) and transversal (b) MSD of polymers of various contour lengths in a solution with a constant mesh size of  $\xi \approx 1.57$ . The curves in the upper figure are numbered according to the Tab. 3.2. Additional axis indicates the change in the polymer contour length  $L$  from simulation to simulation. The slope of the curve 1 in the upper figure obtained by fitting gives the doubled longitudinal diffusion coefficient according to the Eq. 3.3.

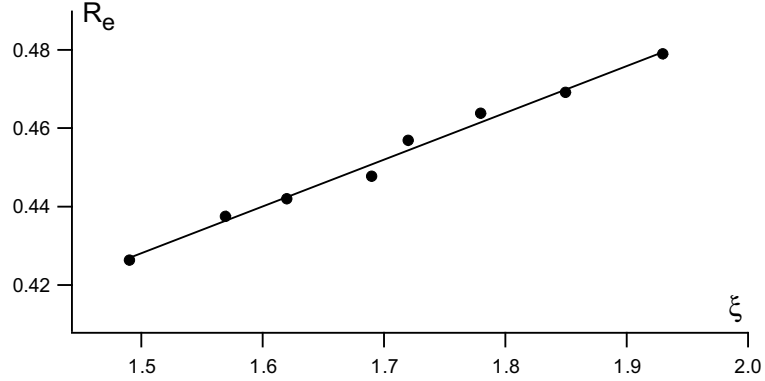


Figure 3.7: Dots: the average radius of the fluctuation tube  $R_e$  as a function of the mesh size  $\xi$ . The solid line is a linear fit of the data.

a way are plotted against the polymer contour length  $L$  in the log-log scale in the Fig. 3.8. The solid line, which is a linear fit of the data, has a slope  $-1.0037$ . It shows, therefore, that the longitudinal diffusion coefficient of polymers in solution is inversely proportional to the polymer contour length

$$D_{\parallel} \sim \frac{1}{L}, \quad (3.4)$$

which is in accord with the Eq. 3.1.

### 3.3 The dissipative force constant $\gamma_{\text{mw}}$ of monomer-water interaction controls the longitudinal diffusion coefficient of polymers

It is natural to assume that the monomer-water dissipative force constant determines the diffusion coefficient of polymers, which is the case for a Brownian particle. Whereas it is not our aim to obtain the exact dependence of the diffusion coefficient of polymers on the monomer-water dissipative interaction constant  $\gamma_{\text{mw}}$ , in this section we determine the diffusion coefficients of 70 monomers long polymers for the values of  $\gamma_{\text{mw}}$  used in the active microrheology simulations in the Sec. 2.5.8.

The mesh size of the polymer network in these simulations is  $\xi \approx 1.57$  and the monomer-water dissipative interaction constant takes the values  $\gamma_{\text{mw}} = 0.2, 0.4$  and  $0.7$ . Together with the simulation 2 from the Tab. 3.1, where  $\gamma_{\text{mw}} = 1$ , we have a set of four simulations with different  $\gamma_{\text{mw}}$ .

The transversal mean square displacements of polymers for the taken values of  $\gamma_{\text{mw}}$  are shown in the Fig. 3.9. It can be seen that the saturation

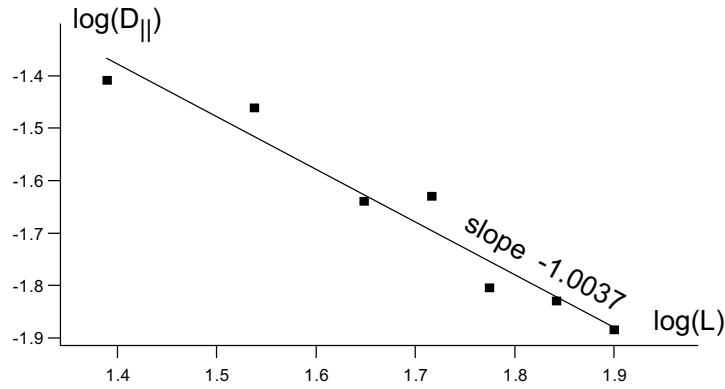


Figure 3.8: The dots represent the longitudinal diffusion coefficient  $D_{\parallel}$  of polymers obtained by fitting the linear regime of the longitudinal MSD  $R_{\parallel}^2$  as shown in the Fig. 3.6 as a function of the polymer contour length  $L$ . The solid line is a linear fit of the data. The slope of  $-1.0037$  indicates that  $D_{\parallel}$  is inversely proportional to  $L$ .

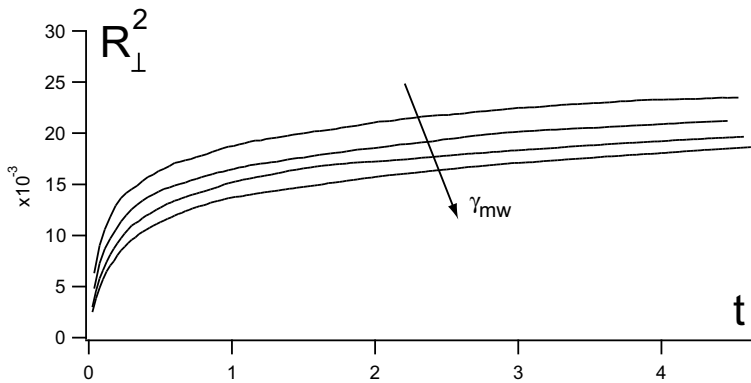


Figure 3.9: Transversal mean square displacements of 70 monomers long polymers. The monomer-water dissipative interaction constant  $\gamma_{mw}$  in these simulations takes the values 0.2, 0.4, 0.7, and 1. The mesh size is  $\xi \approx 1.57$ .

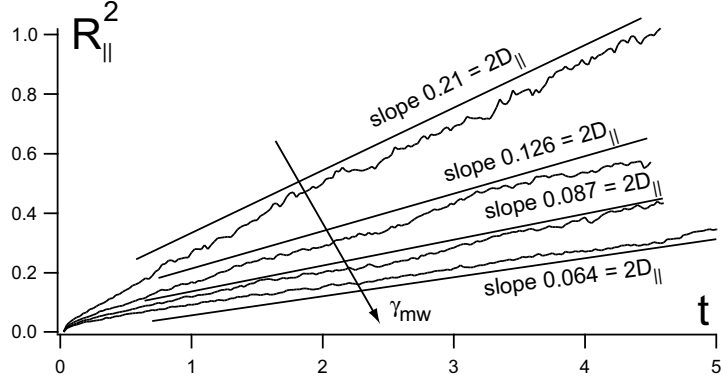


Figure 3.10: Longitudinal mean square displacements of 70 monomers long polymers. The monomer-water dissipative interaction constant  $\gamma_{mw}$  in these simulations takes the values 0.2, 0.4, 0.7, and 1. The mesh size is  $\xi \approx 1.57$ .

time of the transversal MSD decreases with decreasing  $\gamma_{mw}$  in qualitative accordance with the scaling of the entanglement time  $\tau_e$ , Eq. 1.9.

The longitudinal mean square displacements of polymers are shown in the Fig. 3.10. The longitudinal diffusion coefficient  $D_{\parallel}$ , thus, increases with decreasing  $\gamma_{mw}$ . The diffusion coefficients  $D_{\parallel}$  are summarized in the Tab. 3.3.

Table 3.3: Longitudinal diffusion coefficients  $D_{\parallel}$  of 70 monomers long polymers corresponding to the dissipative force constants  $\gamma_{mw}$  of monomer-water interaction.

$\gamma_{mw}$	0.2	0.4	0.7	1.0
$D_{\parallel}$	0.105	0.063	0.044	0.032

# Chapter 4

## Motion of polymers in front of the bead

In this chapter we will determine the character of the polymer motion in front of the bead in the square root regime and compare it with the results of the previous chapter.

The analysis has been made as follows. At time  $t = 6.5$  of the simulation represented by the curve 4 in the Figs. 2.9 and 2.10 the monomers in the cylindrical region in front of the bead (shown in the Fig. 4.1) have been determined. The mesh size in this simulation  $\xi \approx 1.57$ , the external force applied to the bead is  $f = 1000$ , and the radius of the bead is  $R_b = 10$ . At  $t = 6.5$ , as can be seen from the Fig. 2.10, the bead is in the square root regime of motion. The length of the generatrix of this cylindrical region has been taken to be 4, which is comparable with the distance travelled by the bead from the beginning of the simulation. The radius of the section of the cylinder is equal to that of the bead. Therefore, the tracked monomers are those with the coordinates at  $t = 6.5$  satisfying the conditions  $10 < y < 14$  and  $x^2 + z^2 < R_b^2$  whereas the origin of the coordinate system is located in the center of the bead.

The first part of the analysis of the motion of polymers has been done in the following way. The averaged 'y' coordinate of the tracked monomers  $\langle y(t) \rangle$  has been stored during the simulation. The average displacement of the tracked monomers from the beginning of observation is given by  $\langle y(t + 6.5) - y(t = 6.5) \rangle$ . This displacement during approximately 1.5 time units is shown in the Fig. 4.2.

A function of the form  $A\sqrt{t}$  with  $A \approx 0.167$  provides a good fit of the data. The form of the fitting function suggests that the motion of the monomers

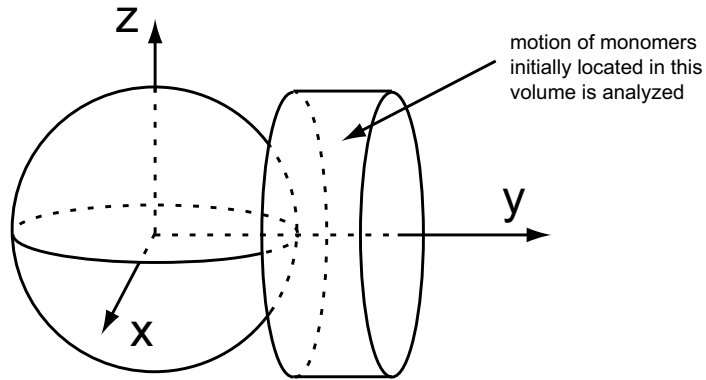


Figure 4.1: We analyze the motion of monomers which at the moment of time  $t = 6.5$  were located in front of the bead in the region shown by the cylinder. The bead moves under an externally applied force in the positive  $Oy$  direction.

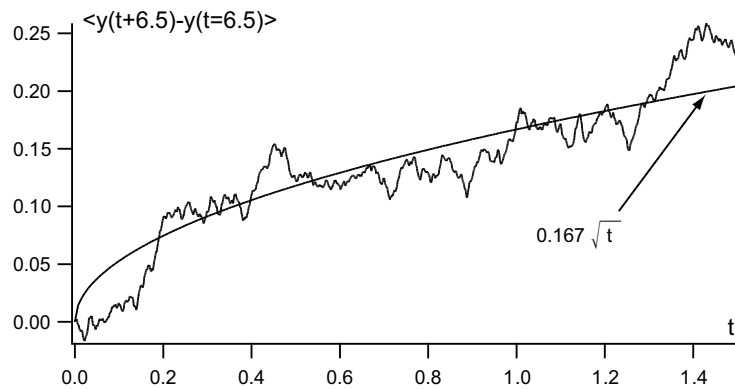


Figure 4.2: Displacement of monomers in front of the bead moving in the square root regime and a fit  $0.167\sqrt{t}$  to the data.

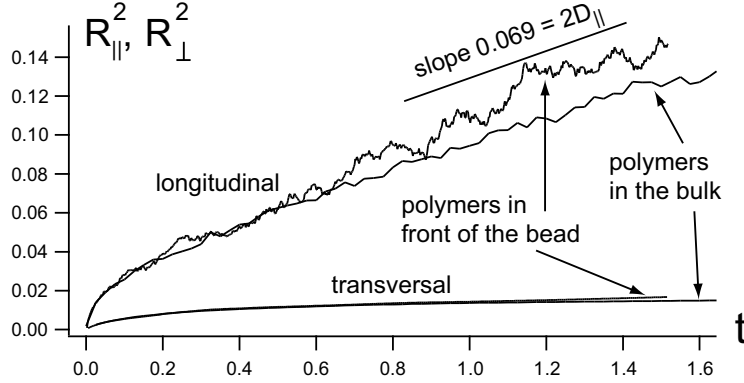


Figure 4.3: Longitudinal and transversal mean square displacements of segments of polymers formed by the tracked monomers in front of the bead. The same data for the diffusion of polymers in the bulk is shown.

in front of the bead is diffusive with the diffusion coefficient being

$$D \sim \frac{A^2}{2} \approx 0.014. \quad (4.1)$$

This value is very close to the longitudinal diffusion coefficient  $D_{\parallel} \approx 0.032$  of the polymers of the same length in a solution with the same concentration obtained as described in the Ch. 3. It is smaller, though, than  $D_{\parallel}$  due to the fact that the polymers are only able to diffuse along their fluctuation tubes, i.e. their diffusion is effectively one-dimensional, and that the tracked monomers form segments of polymers, which not necessarily lie parallel to the Oy axis, i.e. parallel to the direction of the enforced bead movement.

The same type of analysis as performed in the Ch. 3 for the study of longitudinal and transversal diffusion of polymers in solutions has been employed to study the motion of the segments of polymers formed by the tracked monomers in front of the bead. The results for the longitudinal and transversal MSDs of segments of polymers in front of the bead are shown in the Fig. 4.3. For comparison the data for the diffusion of polymers in the bulk are shown in the same graph, which is obtained as described in the Ch. 3 for the same polymer contour length as in the enforced bead motion simulation and at the same polymer concentration.

The good coincidence of the two data sets allows one to infer that the motion of polymers in front of the bead is similar to that in the bulk. It follows that the transversal motion of polymers is hindered by the neighboring polymers and that the polymers experience longitudinal diffusion. The longitudinal diffusion coefficient of polymers in front of the bead is close to that in the bulk as can be inferred from the Fig. 4.3.



# Chapter 5

## Power laws of the compliance and the relaxation modulus in $t$ and $\omega$ domains

As it has been mentioned in the introduction Ch. 1 the compliance of actin networks measured in recent active microrheological experiments [37] is not in accord with the behavior shown in the Fig. 1.4b, which corresponds to the relaxation modulus sketched in the Fig. 1.4a and to the complex modulus behavior depicted in the Fig. 1.3. In this chapter we find the complex relaxation modulus  $G^*(\omega)$  corresponding to the compliance behavior observed in [37] and shown in the Fig. 1.5 as well as we find the scaling of the relaxation modulus  $G(t)$  corresponding to the square root dependence behavior of the compliance.

Recent active microrheological experiments [37], as described in the Sec. 1.3.3, reveal that the compliance of the tightly-entangled actin networks can be sketched as shown in the Fig. 5.1. Thus, the compliance possesses three distinct regimes described in the Sec. 1.3.3. The relaxation modulus  $G(t)$  corresponding to the compliance sketched in the Fig. 5.1a as well possesses three distinct regimes. The compliance in the Fig. 5.1 is given by  $J(t) = A_1 t^{0.75}$  at times  $t < \tau_1$ . Therefore, as in the Fig. 1.4a, the relaxation modulus  $G(t)$  experiences the power law  $t^{-0.75}$ , Fig. 5.1b. This can be shown using the convolution identity Eq. 1.4, which is satisfied when the relaxation modulus is given by

$$G(t) = \frac{2\sqrt{2}}{3\pi A_1 t^{0.75}}. \quad (5.1)$$

In order to find out the behavior of the relaxation modulus corresponding to the square root regime of the compliance we consider the convolution identity 1.4 at times  $\tau_1 \ll t < \tau_2$ , which is possible since in the experiments

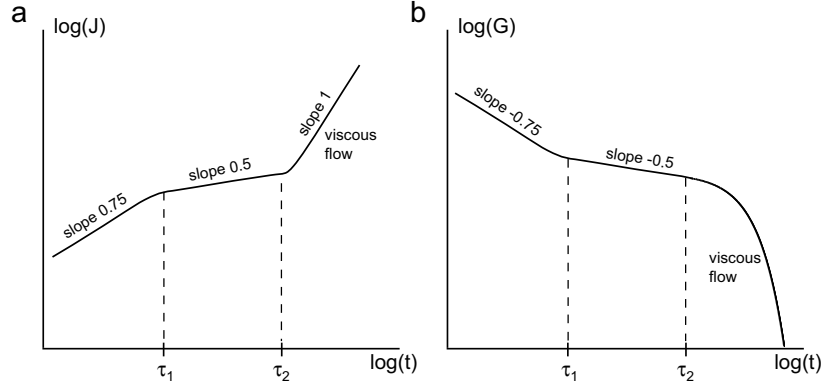


Figure 5.1: (a) A sketch of the compliance  $J(t)$  of actin networks as measured in the active microrheological experiments [37]. (b) A sketch of the relaxation modulus  $G(t)$  corresponding to the compliance in the shown left figure.

this regime spans two orders of magnitude in time [37]. The identity 1.4 can be rewritten as

$$\int_0^{\tau_1} G(t-t') J(t') dt' + \int_{\tau_1}^t G(t-t') J(t') dt' = t. \quad (5.2)$$

Because the relaxation modulus  $G(t)$  is a decreasing function of time the first integral in the left hand side of the Eq. 5.2 can be majorized as

$$\int_0^{\tau_1} G(t-t') J(t') dt' < \int_0^{\tau_1} G(\tau_1-t') J(t') dt' = \tau_1. \quad (5.3)$$

Therefore, since  $t \gg \tau_1$  we can neglect this term in 5.2.

Assume that the compliance is given by

$$J(t) = A_2 \sqrt{t}. \quad (5.4)$$

Then under the assumption  $t \gg \tau_1$  the relaxation modulus

$$G(t) = \frac{2}{\pi A_2 \sqrt{t}} \quad (5.5)$$

satisfies the identity 5.2, because under the assumption  $t \gg \tau_1$

$$\int_{\tau_1}^t \frac{2}{\pi \sqrt{t-t'}} \sqrt{t'} dt' = t + \frac{2}{\pi} \sqrt{\tau_1(t-\tau_1)} - \frac{2t}{\pi} \operatorname{arccot} \sqrt{\frac{t}{\tau_1} - 1} \approx t \quad (5.6)$$

Consequently, at times  $\tau_1 < t < \tau_2$  the relaxation modulus is a power law  $G(t) \sim t^{-0.5}$ . Analogously it can be shown that at times  $t \gg \tau_2$ , when

the compliance is proportional to time  $J(t) \sim t$ , the relaxation modulus experiences an exponential decay corresponding to a viscous flow. Therefore, the relaxation modulus  $G(t)$  corresponding to the compliance shown in the Fig. 5.1a can be sketched as depicted in the Fig. 5.1b.

The relaxation modulus  $G(t)$  determined from the measurement of the compliance [37] (Fig. 1.5) experiences thus no plateau. It shows the initial  $\sim t^{-0.75}$ , intermediate  $\sim t^{-0.5}$  and long time viscous regimes. Therefore, the corresponding complex modulus  $G^*(\omega)$  defined by the Eq. 1.2 as well experiences no elastic plateau in the frequency interval  $\tau_2^{-1} < \omega < \tau_1^{-1}$ . Taking into account that

$$i\omega \int_0^\infty \frac{1}{\sqrt{t}} e^{-i\omega t} dt \sim \omega^{1/2}, \quad (5.7)$$

it can be found that both the storage and the loss moduli scale with frequency as  $\omega^{0.5}$  in the frequency range  $\tau_2^{-1} < \omega < \tau_1^{-1}$ , while at high frequencies  $\omega > \tau_1^{-1}$  they scale as  $\omega^{0.75}$  and at low frequencies  $\omega < \tau_2^{-1}$  the storage and the loss moduli scale as  $G'(\omega) \sim \omega^2$  and  $G''(\omega) \sim \omega$ , which corresponds to the viscous behavior.

Here we suggest a simple ansatz to calculate the complex relaxation modulus  $G^*(\omega)$  from the compliance measured in the active microrheological experiments. A response of the bead on the constant external force measured in [37] is shown in the Fig. 5.2a. The three distinct regimes described above are clearly seen in the Fig. 5.2b. The displacement of the bead is proportional to the compliance  $J(t)$  in the case of a constant applied external force [62]

$$J(t) = \frac{6\pi R}{f} x(t), \quad (5.8)$$

where  $R$  is the radius of the bead and  $f$  is the applied external force. Therefore, one can determine the complex relaxation modulus  $G^*(\omega)$  corresponding to the compliance in the Fig. 5.2a in the following way.

First of all, we fit the compliance of the bead with an analytical function, the form of which can be chosen taking into consideration the different regimes experienced by the compliance, Fig. 5.2b. The only requirement is that, as we will see, the fitting function permits an analytical Laplace transform. We choose the fitting function in the form

$$J(t) = A_1 t^{3/4} e^{-t/\tau_1} + A_2 t^{1/2} (1 - e^{-t/\tau_1}) e^{-t/\tau_2} + (a + A_3 t) (1 - e^{-t/\tau_2}), \quad (5.9)$$

where  $A_1$ ,  $A_2$ ,  $a$ ,  $A_3$ ,  $\tau_1$  and  $\tau_2$  are the fitting parameters. The three terms of the Eq. 5.9 describe the three consequent regimes and the numeration of

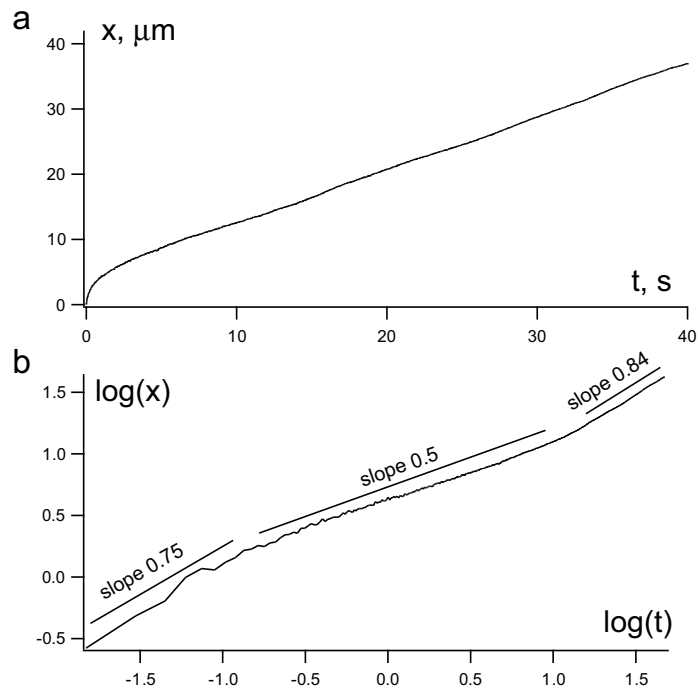


Figure 5.2: (a) Response of a  $4.5 \mu\text{m}$  diameter bead on a constant external force of 15 pN in an actin network solution with the mesh size  $\xi \approx 0.5 \mu\text{m}$  measured in [37]. (b) The same data shown in the log-log scale. The bead exhibits the initial  $x \sim t^{0.75}$  regime followed by the  $x \sim t^{0.5}$  law of motion spanning over two orders of magnitude in time. The square root regime changes to viscous like motion at later times. With a kind permission of Jörg Uhde.

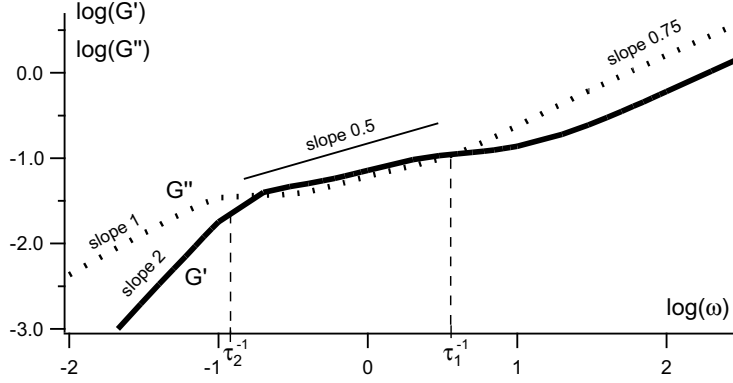


Figure 5.3: The storage  $G'$  (solid line) and the loss  $G''$  (dashed line) moduli corresponding to the compliance from the Fig. 5.2 obtained by fitting with the function 5.9 and utilizing the Eq. 5.12.

the coefficients  $A_i$  corresponds to that given in 1.15. The Laplace transform of the fitting function 5.9 is given by

$$\begin{aligned} \tilde{J}(s) = & A_1 \frac{\Gamma\left(\frac{7}{4}\right)}{(s + \tau_1^{-1})^{7/4}} + A_2 \frac{\sqrt{\pi}}{2} \left( \frac{1}{(s + \tau_2^{-1})^{3/2}} - \frac{1}{(s + \tau_1^{-1} + \tau_2^{-1})^{3/2}} \right) \\ & + \frac{a\tau_2^{-1}}{s(s + \tau_2^{-1})} + \frac{A_3\tau_2^{-1}(2s + \tau_2^{-1})}{s^2(s + \tau_2^{-1})^2}, \end{aligned} \quad (5.10)$$

where  $\Gamma(x)$  is the Gamma function.

The Laplace transform  $\tilde{G}(s)$  of the relaxation modulus  $G(t)$  can be obtained from the identity 1.4, which can be rewritten as

$$s^2 \tilde{G}(s) \tilde{J}(s) = 1. \quad (5.11)$$

Taking into account the Eq. 1.2 we obtain for the complex relaxation modulus

$$G^*(\omega) = \frac{1}{i\omega \tilde{J}(i\omega)}. \quad (5.12)$$

The fitting of the data shown in the Fig. 5.2 with the fitting function 5.9 gives the characteristic times  $\tau_1 \approx 0.29$  s and  $\tau_2 \approx 8.33$  s and the amplitudes  $A_1 \approx 18.86$  Pa $^{-1} \cdot$  s $^{-3/4}$ ,  $A_2 \approx 11.23$  Pa $^{-1} \cdot$  s $^{-1/2}$ ,  $a \approx 12.49$  Pa $^{-1}$  and  $A_3 \approx 2.32$  Pa $^{-1} \cdot$  s $^{-1}$ . The real and the imaginary parts of the complex modulus  $G^*(\omega)$  corresponding to the compliance from the Fig. 5.2 are shown in the Fig. 5.3. Thus, as asserted above the square root time dependence of the compliance corresponds to the  $\omega^{1/2}$  scaling of both the relaxation and the loss moduli.

At frequencies  $\omega > \tau_1^{-1}$  the storage and the loss moduli  $G'(\omega)$  and  $G''(\omega)$  scale as  $\omega^{3/4}$ , Fig. 5.3. Consequently, as asserted in [37] the characteristic time  $\tau_1$  can be identified with the characteristic time  $\tau_e$  of single filament dynamics.

At the same time, the characteristic time of the system to reach a steady state velocity (viscous flow regime)  $\tau_2$  is at least 2 orders of magnitude shorter than the characteristic time  $\tau_{\text{rep}}$  measured in experiments [29, 30, 32, 33], which takes the values 1000 s and longer.

# Chapter 6

## Osmotic force

The computer simulations described in the chapters 2, 3 and 4 enable us to make the following conclusions about the motion of the bead in active microrheological experiments on semiflexible polymer solutions

- The square root regime of the motion of the bead is correlated with the increase of the polymer concentration in front of the bead and a significant decrease behind it
- The resistance force experienced by the bead is mainly due to the surrounding polymers, i.e. the water contribution to the resistance force is negligible
- The motion of the polymers in front of the moving bead is similar to that in the bulk, i.e. they move by means of longitudinal diffusion with the diffusion coefficient being very close to that in the bulk

On the basis of our simulations we suggest the following scaling theory of the active microrheology of semiflexible polymer solutions.

### 6.1 Osmotic pressure of polymers

Consider a semiflexible polymer with contour length  $L$  confined to a reptation tube Fig. 6.1. As it has been asserted in [60, 63–66], the segments of polymers of length  $L_e$  contribute a value of the order of  $k_B T$  to the free energy of the polymer. Therefore, the free energy of the polymer is proportional to the number of segments of length  $L_e$  in the polymer. Using the Eqs. 1.6, 2.13 and 1.8 we find

$$L_e \sim L_p^{1/3} \xi^{2/3}. \quad (6.1)$$

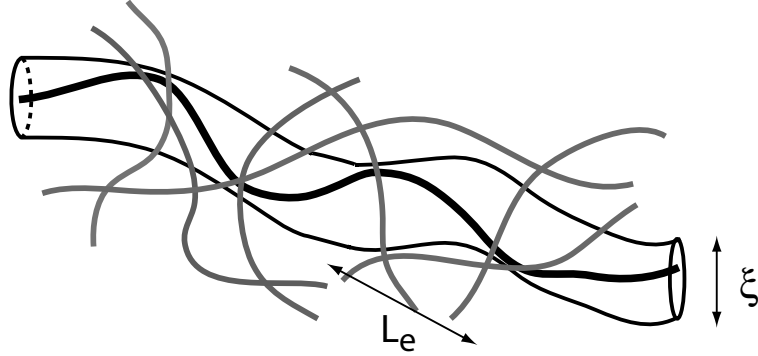


Figure 6.1: Reptation tube of a semiflexible polymer in solution.

Thus, the free energy of a confined polymer can be written in the form

$$F_1 = \gamma k_B T \frac{L}{L_p^{1/3} \xi^{2/3}}, \quad (6.2)$$

where  $\gamma \approx 2.46$  has been estimated from computer simulations [65].

The pressure exerted by the polymer on the walls of the confining tube can be calculated in the following way. Assume that there are  $N$  polymers of length  $L$  in the volume  $V$ . The free energy of the polymers is given by

$$F = NF_1 = \gamma k_B T \frac{(NL)^{4/3}}{L_p^{1/3} (3V)^{1/3}}, \quad (6.3)$$

where we have used Eq. 2.13 for the mesh size of the network. The pressure is then given by

$$p = -\frac{\partial F}{\partial V} = \gamma k_B T \frac{(NL)^{4/3}}{L_p^{1/3} (3V)^{4/3}}. \quad (6.4)$$

Introducing the concentration of segments of length  $L_e$

$$c^* = \frac{NL}{L_e V} = \frac{3}{L_p^{1/3} \xi^{8/3}}, \quad (6.5)$$

where the Eqs. 6.1 and 2.13 have been used, we can rewrite the osmotic pressure of polymers Eq. 6.4 in a simple form

$$p = \frac{\gamma}{3} c^* k_B T. \quad (6.6)$$

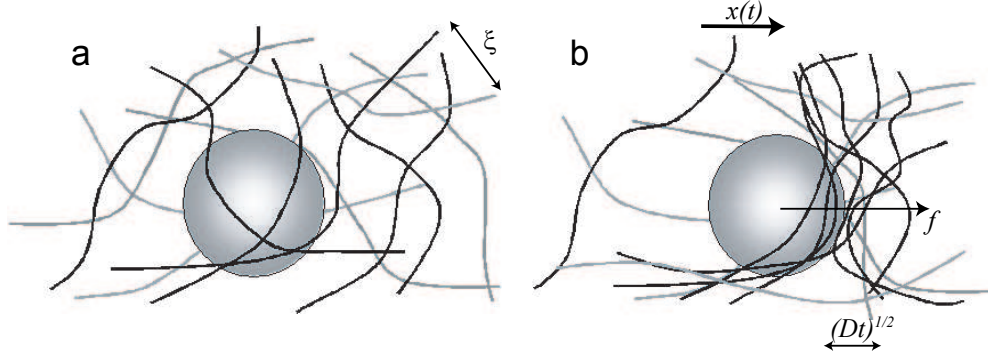


Figure 6.2: (a) A bead in a solution of semiflexible polymers. (b) An external force  $f$  applied on the bead causes its displacement  $x(t)$ . The polymer network is deformed resulting in an increased concentration of polymers in front of and decreased behind the bead.

## 6.2 Osmotic resistance force

At the moment of application of an external force  $f$  on the bead the distribution of polymers around it is homogeneous, Fig. 6.2a (*cf.* also Fig. 2.8a). The applied force causes the displacement of the bead leading to the deformation of the polymer network, Fig. 6.2a. As it has been shown in the Sec. 2.5.3 the concentration of polymers in front of the bead is higher than that in the bulk, whereas the concentration behind the bead is much lower than in the bulk, *cf.* also Fig. 2.8c. In the Sec. 2.5.4 it has been shown that the bead experiences an osmotic resistance force due to the difference in the polymer concentration in front of and behind the bead, and that the viscous contribution is negligible. Therefore, the external force is balanced by the osmotic resistance force

$$f \sim p \cdot \pi R^2 \sim \frac{\gamma\pi}{3} c^* k_B T R^2, \quad (6.7)$$

where we have used  $\pi R^2$  for the section area of the front hemisphere of the bead.

## 6.3 Motion of the bead

It has been found in the Ch. 4, that the motion of polymers in front of the bead is similar to that in the bulk, i.e. the polymers move by means of the longitudinal diffusion with the same diffusion coefficient  $D_{||}$  as in the bulk. Therefore, the polymers can be described with the help of the diffusion

equation

$$\frac{\partial c}{\partial t} = D_{\parallel} \Delta c, \quad (6.8)$$

where  $c$  is the polymer concentration

$$c = \frac{3}{L\xi^2}. \quad (6.9)$$

### 6.3.1 Square root regime

Consider a bead moving in such a diffusing medium under an applied external force  $f$ , Fig. 6.2. Let us assume that within time  $t$  the bead displaces a distance  $x(t)$ . During its motion the bead rakes up polymers in front of itself. The number of polymers raked up within the distance  $x(t)$  is given by

$$N = c_0 \pi R^2 x(t), \quad (6.10)$$

where  $c_0$  is the concentration of polymers far from the bead, where the mesh size is  $\xi_0$ . Within the time  $t$  the polymers diffuse a distance  $\sqrt{D_{\parallel}t}$  and spread, thus, over the volume  $\pi R^2 \sqrt{D_{\parallel}t}$ , Fig. 6.2b. Therefore, the concentration right in front of the bead is given by

$$c \sim \frac{N}{\pi R^2 \sqrt{D_{\parallel}t}} \sim \frac{x(t)}{\sqrt{D_{\parallel}t}} c_0. \quad (6.11)$$

From the Eqs. 6.5 and 6.9 we find the relation between the concentrations  $c$  and  $c^*$

$$c = \frac{L_p^{1/3} \xi^{2/3}}{L} c^*. \quad (6.12)$$

Assuming that the deformation  $\delta\xi$  of the polymer network is small, i.e.  $\delta\xi/\xi_0 \approx 0$ , we can use  $\xi = \xi_0$  in the Eq. 6.12. Combining the Eqs. 6.5, 6.11 and 6.12 we find

$$c^* \sim \frac{3x(t)}{L_p^{1/3} \xi_0^{8/3} \sqrt{D_{\parallel}t}} c_0. \quad (6.13)$$

Finally, using the Eqs. 6.7, 6.9 and 6.13 we find that the displacement of the bead is given by

$$x \sim \frac{L_p^{1/3} \xi_0^{8/3} f \sqrt{D_{\parallel}}}{\gamma \pi R^2 k_B T} \sqrt{t}. \quad (6.14)$$

### 6.3.2 Steady state regime

If  $t > \tau_2 = R^2/2D_{\parallel}$  the polymers have time to diffuse sideways and escape the path of the bead. In this case the motion of the bead is steady. Assume that the bead moves with a constant velocity  $v$ . The number of polymers  $N_+$  raked up by the bead within the time  $\Delta t$  is given by

$$N_+ \sim \pi R^2 v \Delta t c_0. \quad (6.15)$$

In front of the bead a region with concentration  $c$  is formed which is higher than that in the bulk. The flux of polymers diffusing away from that region  $\vec{j} = -D_{\parallel} \nabla c$  can be estimated as

$$j \sim -\frac{D_{\parallel} c}{R}, \quad (6.16)$$

where we assume that the size of the region of increased concentration is of the order of the size of the bead  $R$ . Thus, the number of polymers  $N_-$  escaping this region sideways within the time  $\Delta t$  is

$$N_- \sim -2\pi R^2 j \Delta t \sim 2\pi R D_{\parallel} c \Delta t. \quad (6.17)$$

In the steady state the numbers of raked up polymers and those diffusing away from the bead's path are equal  $N_+ = N_-$  and we obtain for the velocity of the bead

$$v \sim \frac{2D_{\parallel} c}{R c_0}. \quad (6.18)$$

Using the Eqs. 6.5, 6.7, 6.12 and 6.18 we find that the velocity of the bead is given by

$$v \sim \frac{2L_p^{1/3} \xi_0^{8/3} D_{\parallel}}{\gamma \pi R^3 k_B T} f. \quad (6.19)$$

### 6.3.3 Characteristic time of the square root regime

Deriving the displacement of the bead in the square root regime Eq. 6.14 with respect to time we find the velocity of the bead in the square root regime

$$v = \frac{L_p^{1/3} \xi_0^{8/3} f \sqrt{D_{\parallel}}}{2\gamma \pi R^2 k_B T \sqrt{t}}. \quad (6.20)$$

Comparing it with the velocity in the steady state Eq. 6.19 we find that the characteristic time of emerging of the steady state regime is given by

$$\tau_2 = \frac{R^2}{2D_{\parallel}}, \quad (6.21)$$

which is, thus, the characteristic time for a polymer to diffuse a distance of the order of the size of the bead.

## 6.4 Comparison with the experiments

In this section we compare the scaling results on the osmotic force mechanism of this chapter with the experimental values obtained by the fitting procedure in the Ch. 5. Using the Eq. 5.8 we get from the Eq. 6.14 the amplitude  $A_2$  of the square root regime of the bead motion

$$A_2 = \frac{6L_p^{1/3}\xi^{8/3}\sqrt{D_{\parallel}}}{\gamma R k_B T}. \quad (6.22)$$

The longitudinal diffusion coefficient of polymers is given by

$$D_{\parallel} = \frac{k_B T}{\zeta_{\parallel} L}, \quad (6.23)$$

where  $\zeta_{\parallel}$  is given by the Eq. 3.1. Inserting the values  $\xi \approx 0.3 \mu\text{m}$ ,  $L \approx 20 \mu\text{m}$ ,  $R \approx 2.25 \mu\text{m}$  into the Eq. 6.22 we find  $A_2 \approx 9.2 \text{ Pa}^{-1} \cdot \text{s}^{-1/2}$  in excellent agreement with the experimental value  $A_2 \approx 11.23 \text{ Pa}^{-1} \cdot \text{s}^{-1/2}$ , Ch. 5.

In the steady state we find

$$A_3 = \frac{12L_p^{1/3}\xi^{8/3}D_{\parallel}}{\gamma R^2 k_B T}. \quad (6.24)$$

Inserting the same values gives  $A_3 \approx 2.7 \text{ Pa}^{-1} \cdot \text{s}^{-1}$  in agreement with the measured experimental value  $A_3 \approx 2.32 \text{ Pa}^{-1} \cdot \text{s}^{-1}$ .

Finally, for the characteristic time  $\tau_2$  we find  $\tau_2 \approx 23 \text{ s}$ , which is in the same order of magnitude with the characteristic time  $\tau_2 \approx 8.33 \text{ s}$  of the emerging of the steady state in the active microrheological experiments.

## 6.5 Comparison with the computer simulations

As shown in the Sec. 6.3.1 the displacement of the bead in the square root regime is given by  $x = A\sqrt{t}$  with

$$A = \frac{L_p^{1/3}\xi^{8/3}f\sqrt{D_{\parallel}}}{\gamma\pi R^2 k_B T}. \quad (6.25)$$

Using the Eqs. 1.6 and 2.13 one finds  $A \sim \rho^{-4/3}f\sqrt{D_{\parallel}}$  in perfect agreement with the results of the computer simulations presented in the sections 2.5.5, 2.5.6 and 2.5.8. The theoretical scaling  $A \sim R^{-2}$  is close to  $A \sim R^{-8/5}$  obtained by computer simulations, Sec. 2.5.7.

Substituting the values  $\xi = 1.57$ ,  $L = 34.5$ ,  $R = 10$ ,  $L_p = 150$ ,  $k_B T = 1$ ,  $f = 1000$  and  $D_{||} = 0.032$  in the Eq. 6.25 we find  $A \approx 4.1$ , which is in a good agreement with the value  $A \approx 1.7$  obtained by computer simulations.

For the characteristic time of the square root regime we find  $\tau_2 \approx 10^3$  time units. Since the typical simulations time was about 5 time units, the steady state regime of the bead motion has not been reached. Whether this regime can be simulated with the present computer facilities should be a subject of additional work.



# Chapter 7

## Steady state regime: asymptotic analytical solution

The scaling estimates of the Ch. 6 show that semiflexible polymer networks in active microrheological experiments can be described with the help of the diffusion equation

$$\frac{\partial c}{\partial t} = D_{||} \Delta c. \quad (7.1)$$

In this chapter we consider the steady state regime of the motion of the bead analytically. For this purpose we first derive the diffusion equation for the concentration  $c^*$  of segments of polymers of length  $L_e$ .

Applying the Laplace operator to the Eqs. 6.9 and 6.5 we find

$$\Delta c = -\frac{6}{L\xi^3} \Delta \xi \quad (7.2)$$

$$\Delta c^* = -\frac{8}{L_p^{1/3} \xi^{11/3}} \Delta \xi, \quad (7.3)$$

where we have neglected the terms proportional to  $(\nabla \xi)^2$  assuming the deformation of the polymer network to be small. Therefore, we find

$$\frac{\Delta c}{\Delta c^*} = \frac{3L_p^{1/3} \xi^{2/3}}{4L}. \quad (7.4)$$

Taking the time derivative of the Eqs. 6.9 and 6.5 we find

$$\dot{c} = -\frac{6}{L\xi^3} \dot{\xi} \quad (7.5)$$

$$\dot{c}^* = -\frac{8}{L_p^{1/3} \xi^{11/3}} \dot{\xi}. \quad (7.6)$$

Therefore,

$$\frac{\dot{c}}{c^*} = \frac{3L_p^{1/3}\xi^{2/3}}{4L}. \quad (7.7)$$

Combining the Eqs. 7.4, 7.7 and 7.1 we find that in the linear regime the concentration  $c^*$  satisfies the same diffusion equation

$$\frac{\partial c^*}{\partial t} = D_{||}\Delta c^*. \quad (7.8)$$

We assume that in the regime of the steady motion of the bead the system is characterized by a steady concentration distribution of polymers around the bead. The latter moves with constant velocity  $\vec{v}$ . It is more convenient to tackle the problem in the coordinate frame connected with the bead  $c(\vec{r}, t) = c(\vec{r} - \vec{v}t, t)$ . Thus, the Eq. 7.8 takes the form

$$D_{||}\Delta c^* - \vec{v} \cdot \nabla c^* = 0. \quad (7.9)$$

We utilize a spherical coordinate system  $(r, \theta, \varphi)$  as shown in the Fig. 2.12. The external force applied to the bead is  $f$  and the velocity of polymers at infinity is

$$\vec{v} = (-v \cos \theta, v \sin \theta, 0), \quad v > 0. \quad (7.10)$$

The concentration of polymers at infinity is constant, therefore the first boundary condition is

$$c^*(r = \infty, \theta, \varphi) = c_0^*. \quad (7.11)$$

The second boundary condition is the requirement that the flux of polymers normal to the bead surface vanishes

$$D \left. \frac{\partial c^*}{\partial r} \right|_{r=R} + v c^*(R, \theta, \varphi) \cos \theta = 0. \quad (7.12)$$

The osmotic force experienced by the bead is calculated as an integral of the pressure Eq. 6.6 over the surface of the bead

$$f_{\text{osm}} = \frac{\gamma}{3} k_B T \int_0^{2\pi} \int_0^\pi c^*(R, \theta, \varphi) \cos \theta R^2 \sin \theta d\theta d\varphi \quad (7.13)$$

and the osmotic force should be balanced by the external force in the steady state  $f = f_{\text{osm}}$ .

The general solution of the equation 7.9 satisfying the boundary condition 7.11 takes the form

$$c^*(r, \theta, \varphi) = c_0^* \left( 1 + e^{-kr \cos \theta} \sum_{n=0}^{\infty} B_n \frac{1}{\sqrt{r}} K_{n+1/2}(kr) P_n(\cos \theta) \right), \quad (7.14)$$

where  $P_n(x)$  is the Legendre polynomial,  $K_n(x)$  is the modified Bessel function of the second kind,  $B_n$  are coefficients and

$$k = \frac{v}{2D_{\parallel}}. \quad (7.15)$$

One can expect that the coefficients  $B_n$  decrease with the number  $n$ . Therefore, we keep only the first two modes in the series in the Eq. 7.14 and later justify this truncation. Thus, we have

$$c^*(r, \theta, \varphi) = c_0^* \left( 1 + e^{-kr \cos \theta} \left( B_0 \frac{1}{\sqrt{r}} K_{1/2}(kr) + B_1 \frac{1}{\sqrt{r}} K_{3/2}(kr) P_1(\cos \theta) \right) \right). \quad (7.16)$$

The coefficients  $B_0$  and  $B_1$  are determined by substituting the solution 7.16 into the boundary condition 7.12. Using the identity

$$e^{z \cos \varphi} = \sum_{n=-\infty}^{\infty} I_n(z) \cos n\varphi \quad (7.17)$$

where  $I_n(x)$  is the modified Bessel function of the first kind, we obtain

$$B_0 = \frac{4\sqrt{2}\mu^{3/2}\sqrt{R}e^{\mu}(\mu(1+\mu)I_0(\mu) + (1+\mu(1+\mu))I_1(\mu))}{\sqrt{\pi}(1+\mu)(2+\mu)^2} \quad (7.18)$$

$$B_1 = \frac{4\sqrt{2}\mu^{3/2}\sqrt{R}e^{\mu}(2\mu(1+\mu)I_0(\mu) - (2+\mu(2-\mu))I_1(\mu))}{\sqrt{\pi}(1+\mu)(2+\mu)^2},$$

where  $\mu = kR \equiv vR/2D_{\parallel}$ .

The approximate solution 7.16 with the mode amplitudes given by 7.18 can be regarded as a reasonable approximation under the assumption

$$\mu \equiv \frac{vR}{2D_{\parallel}} < 1 \quad (7.19)$$

since one can calculate the ratio  $B_2/B_1$  as a function of  $\mu$  and find that under this assumption  $B_2/B_1 < 0.15$ . A sketch of the concentration distribution around the bead calculated with the help of the Eq. 7.16 is shown in the Fig. 7.1.

Substituting the solution 7.16 with the amplitudes given by 7.18 into the equation for the osmotic force acting on the bead Eq. 7.13 we find in the first order with respect to  $kR$

$$f_{\text{osm}} = \frac{2\pi\gamma c_0^* k_B T v R^3}{9D_{\parallel}}. \quad (7.20)$$

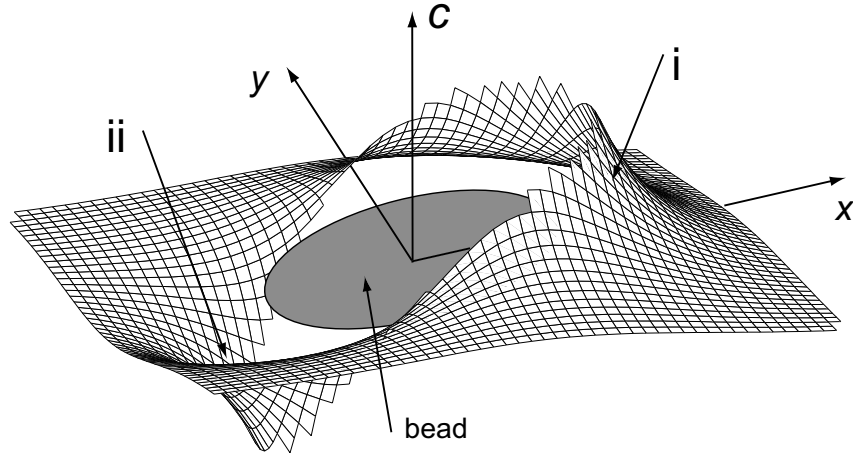


Figure 7.1: A sketch of the polymer concentration distribution around the bead moving with a constant velocity as calculated using Eq. 7.16. The external force is applied along the Ox axes and the  $z = 0$  section is shown. (i) the region of increased concentration of polymers in front of the bead, (ii) the region of decreased concentration of polymers behind the bead.

Therefore, in the first order with respect to  $vR/2D_{\parallel}$  we obtain for the velocity  $v$  of the bead moving in a semiflexible polymer solution under an external force  $f$

$$v = \frac{3L_p^{1/3}\xi^{8/3}D_{\parallel}}{2\pi\gamma R^3 k_B T} f, \quad (7.21)$$

where we have used the Eq. 6.5. This result yields the same behavior as the Eq. 6.19 obtained within the scaling estimates. In addition we obtained here the geometric prefactor.

# Chapter 8

## Conclusions

This treatise has been concerned with the studying of active microrheology of semiflexible polymer solutions. As described in the introduction, Ch. 1, there is a lack of understanding of the viscoelastic properties of semiflexible polymer solutions on the time scales when the mechanical response of the medium becomes governed by the collective dynamics of polymers. Experiments on actin solutions, which has become a prominent model of a semiflexible polymer, show contradictory results. Some groups report the existence of an elastic plateau in the complex relaxation modulus  $G^*(\omega)$  followed by a viscous flow regime. The value of the elastic plateau, however, varies from group to group by as much as two orders of magnitude. Other studies instead of the elastic plateau report a power law behavior of the complex modulus  $G^*(\omega)$ , which is found to vary as  $\omega^\alpha$  with  $\alpha \approx 0.5$ . Recent experiments on active microrheology of actin solutions [37] are in accord with this scaling as shown in the Ch. 5. These experiments reveal that the response of a bead on a constant external force possesses three distinct regimes. At the initial stage the compliance of the bead is a power law  $J(t) \sim t^{0.75}$ . At times greater approximately 0.3 s a square root dependence of the compliance is found  $J(t) \sim \sqrt{t}$ . This regime spans over about two orders of magnitude in time and changes then into a viscous-like motion  $J(t) \sim t$ .

In order to provide a better understanding of active microrheology of semiflexible polymer solutions we studied it by computer simulations using a sort of molecular dynamics method.

The simulation model accounts only for viscous and steric interactions between polymers. In this framework the first two regimes of the compliance are found, Ch 2. The third regime could not be reached apparently due to the lack of the computer power. It is shown that the square root regime of the motion of the bead is characterized by an increased concentration of polymers in front of the bead and a significantly decreased behind. The

simulations show that in this regime the resistance force experienced by the bead is mainly due to the polymers and that the viscous contribution of water is negligible. Furthermore, it is found that the resistance force created by the polymers is due to the difference in concentrations in front of and behind the bead and is, thus, osmotic in origin. The scaling dependence of the amplitude of the compliance in the square root regime on the concentration of polymers is in good agreement with that in experiments.

In order to characterize the motion of polymers in the vicinity of the moving bead, diffusion of semiflexible polymers in the bulk has been studied. By comparing these results with the analysis of the motion of polymers in front of the moving bead it is found that the latter move similar to the polymers in the bulk. Thus, the polymers in front of the moving bead move by means of longitudinal diffusion with the diffusion coefficient being close to that in the bulk.

Based on these findings a scaling theory of the active microrheology of semiflexible polymer solutions is suggested. The polymers are thought to be described by a diffusion equation and the osmotic pressure of polymers due to the suppression of their undulations is taken into account. Both the square root regime as well as the subsequent viscous-like motion of the bead are described by this model. The obtained scaling laws are in excellent agreement with the experimental results as well as with the computer simulations.

Finally, the viscous-like steady regime is tackled analytically. In the limit of small external forces an approximate concentration distribution of polymers around the moving bead is obtained as well as the relation for the velocity of the bead.

## Summary

- We have simulated solutions of semiflexible polymers with viscous and steric interactions
- In this model we established the existence of the square root regime in the microrheology
- The square root regime is correlated with the increase of the polymer concentration in front of the bead and decrease behind it
- The resistance force experienced by the bead in the square root regime is mainly due to polymers and is osmotic in origin
- The bead displacement is linear with respect to the external force and proportional to  $c^{-1.4}$

- Motion of polymers in front of the bead is similar to that in the bulk, they move by means of longitudinal diffusion with the same diffusion coefficient  $D_{||}$
- The compliance is proportional to  $\sqrt{D_{||}}$
- An analytical scaling model accounting for the osmotic pressure of the polymers due to the suppression of their undulations is proposed



# Bibliography

- [1] F. MacKintosh and C. Schmidt. Microrheology. *Current Op. Colloid Interface Sci.*, 4(4):300–307, 1999.
- [2] M. Solomon and Q. Lu. Rheology and dynamics of particles in viscoelastic media. *Current Op. Colloid Interface Sci.*, 6(5-6):430–437, 2001.
- [3] T. Mason and D. Weitz. Optical measurements of frequency-dependent linear viscoelastic moduli of complex fluids. *Phys. Rev. Lett.*, 74(7):1250–1253, 1995.
- [4] J. Harden and V. Viasnoff. Recent advances in dws-based microrheology. *Current Op. Colloid Interface Sci.*, 6:438–445, 2001.
- [5] J. Crocker, M. Valentine, E. Weeks, T. Gisler, P. Kaplan, A. Yodh, and D. Weitz. Two-point microrheology of inhomogeneous soft materials. *Phys. Rev. Lett.*, 85(4):888–891, 2000.
- [6] J. Levine and T. Lubensky. Two-point microrheology and electrostatic analogy. *Phys. Rev. E*, 65:011501, 1995.
- [7] H. Freundlich and W. Seifriz. Über die elastizität von solen und gelen. *Z. Phys. Chem.*, 104:233, 1922.
- [8] F. Amblard, A. Maggs, B. Yurke, A. Pargellis, and S. Leibler. Subdiffusion and anomalous local viscoelasticity in actin networks. *Phys. Rev. Lett.*, 77:4470–4473, 1996.
- [9] M. Keller, J. Schilling, and E. Sackmann. Oscillatory magnetic bead rheometer for complex fluid microrheometry. *Rev. Sc. Instr.*, 72(9):3626–3634, 2001.
- [10] F. Schmidt, F. Ziemann, and E. Sackmann. Shear field mapping in actin networks by using magnetic tweezers. *Eur. Biophys. J. Biophys. Lett.*, 24:348–353, 1996.

- [11] F. Ziemann, J. Rädler, and E. Sackmann. Local measurements of viscoelastic moduli of entangled actin networks using an oscillating magnetic bead micro-rheometer. *Biophys. J.*, 66:2210–2216, 1994.
- [12] A. Bausch, W. Moller, and E. Sackmann. Measurement of local viscoelasticity and forces in living cells by magnetic tweezers. *Biophys. J.*, 76:573–579, 1999.
- [13] A. Bausch, F. Ziemann, A. Boulbitch, K. Jacobson, and E. Sackmann. Local measurements of viscoelastic parameters of adherent cell surfaces by magnetic bead microrheometry. *Biophys. J.*, 75:2038–2049, 1998.
- [14] S. Kuo. Using optics to measure biological forces and mechanics. *Traffic*, 2(11):757–763, 2001.
- [15] L. Landau and E. Lifshitz. *Statistical physics*, volume 5 of *Theoretical physics*. Pergamon Press, 1959.
- [16] N. Tschoegl. *The phenomenological theory of linear viscoelastic behavior*. Springer-Verlag, 1989.
- [17] F. Gittes, B. Mickey, J. Nettleton, and J. Howard. Flexural rigidity of microtubules and actin filaments measured from thermal fluctuations in shape. *J. Cell Biol.*, 120:923, 1993.
- [18] A. Ott, M. Magnasco, A. Simon, and A. Libchaber. Measurement of the persistence length of polymerized actin using fluorescence microscopy. *Phys. Rev. E*, 48:R1642, 1993.
- [19] F. MacKintosh and P. Janmey. Actin gels. *Curr. Opin. Solid State Mater. Sci.*, 2(3):350–357, 1997.
- [20] M. Dichtl and E. Sackmann. Colloidal probe study of short time local and long time reptational motion of semiflexible macromolecules in entangled networks. *New Journal of Physics*, 1:18.1–18.11, 1999.
- [21] M. Dichtl and E. Sackmann. Microrheometry of semiflexible actin networks through enforced single-filament reptation: Frictional coupling and heterogeneities in entangled networks. *PNAS*, 99(10):6533–6538, 2002.
- [22] M. Doi and E. Edwards. *The theory of polymer dynamics*. Oxford science publications, 1989.

- [23] T. Odijk. On the statistics and dynamics of confined or entangled stiff polymers. *Macromolecules*, 16:1340, 1983.
- [24] A. Semenov. Dynamics of concentrated solutions of rigid-chain polymers part 1 - brownian motion of persistent macromolecules in isotropic solution. *J. Chem. Soc. Faraday Trans.*, 86:317, 1986.
- [25] D. Morse. Tube diameter in tightly entangled solutions of semiflexible polymers. *Phys. Rev. E*, 63:031502, 2001.
- [26] D. Morse. Viscoelasticity of concentrated isotropic solutions of semiflexible polymers. 1. Model and stress tensor. *Macromolecules*, 31:7030–7043, 1998.
- [27] T. Gisler and D. Weitz. Scaling of the microrheology of semidilute F-actin solutions. *Phys. Rev. Lett.*, 82(7):1606–1609, 1999.
- [28] F. Gittes, B. Schnurr, P. Olmsted, F. MacKintosh, and C. Schmidt. Microscopic viscoelasticity: shear moduli of soft materials determined from thermal fluctuations. *Phys. Rev. Lett.*, 79(17):3286–3289, 1997.
- [29] J. Xu, A. Palmer, and D. Wirtz. Rheology and microrheology of semiflexible actin solutions: actin filament networks. *Macromolecules*, 31:6486–6492, 1998.
- [30] J. Xu, V. Viasnoff, and D. Wirtz. Compliance of actin filament networks measured by particle-tracking microrheology and diffusing wave spectroscopy. *Rheol Acta*, 37:387–398, 1998.
- [31] D. Morse. Viscoelasticity of concentrated isotropic solutions of semiflexible polymers. 2. Linear response. *Macromolecules*, 31:7044–7067, 1998.
- [32] A. Palmer, T. Mason, J. Xu, S. Kuo, and D. Wirtz. Diffusing wave spectroscopy microrheology of actin filament networks. *Biophys. J.*, 76:1063–1071, 1999.
- [33] P. Janmey, U. Euteneuer, P. Traub, and M. Schliwa. Viscoelastic properties of vimentin compared with other filamentous biopolymer networks. *J. Cell Biol.*, 113:155–160, 1991.
- [34] B. Hinner, M. Tempel, E. Sackmann, K. Kroy, and E. Frey. Entanglement, elasticity, and viscous relaxation of actin solutions. *Phys. Rev. E*, 81(12):2614–2617, 1998.

- [35] H. Isambert and A. Maggs. Dynamics and rheology of actin solutions. *Macromolecules*, 29:1036–1040, 1996.
- [36] J. Xu, W. Schwarz, J. Käs, T. Stossel, P. Janmey, and T. Pollard. Mechanical properties of actin filament networks depend on preparation, polymerization conditions, and storage of actin monomers. *Biophys. J*, 74:2731–2740, 1998.
- [37] J. Uhde. *Mikrorheometrie passiver und aktiver Aktinnetzwerke*. PhD thesis, Technical University of Munich, 2004.
- [38] F. Schmidt. *Mikrorheologie von Netzwerken semiflexibler Biopolymere*. PhD thesis, Technische Universität München, 1999.
- [39] P Hoogerbrugge and J Koelman. Simulating microscopic hydrodynamic phenomena with dissipative particle dynamics. *Europys. Lett.*, 19(3):155–160, 1992.
- [40] P Español, M Serrano, and I Zuniga. Coarse graining of fluids and its relation with dissipative particle dynamics and smoothed particle dynamics. *Int. J. Mod. Phys. C*, 8(4):899–908, 1997.
- [41] C. Marsh. *Theoretical aspects of dissipative particle dynamics*. PhD thesis, University of Oxford, 1998.
- [42] C. Marsh, G. Backx, and M. Ernst. Static and dynamic properties of dissipative particle dynamics. *Phys. Rev. E*, 56:1676, 1997.
- [43] M. Ripoll, M. Ernst, and P. Español. Large scale and mesoscopic hydrodynamics for dissipative particle dynamics. *J. Chem. Phys.*, 115(15):7271–7284, 2001.
- [44] C.C. Liew and M. Mikami. A coarse-grained model for particle dynamics simulations of complex fluids. *Chem. Phys. Lett.*, 368:346–351, 2003.
- [45] M. Whittle and E. Dickinson. On simulating colloids by dissipative particle dynamics: issues and complications. *J. Colloid Interface Sci.*, 242:106–109, 2001.
- [46] P. Coveney and K. Novik. Computer simulations of domain growth and phase separation in two-dimensional binary immiscible fluids using dissipative particle dynamics. *Phys. Rev. E*, 54(5):5134–5141, 1996.

- 
- [47] J. Shillcock and R. Lipowsky. Equilibrium structure and lateral stress distribution of amphiphilic bilayers from dissipative particle dynamics simulations. *J. Chem. Phys.*, 117(10):5048–5061, 2002.
- [48] M. Kranenburg, M. Venturoli, and B. Smit. Molecular simulations of mesoscopic bilayer phases. *Phys. Rev. E*, 67:060901, 2003.
- [49] S. Yamamoto, Y. Maruyama, and S. Hyodo. Dissipative particle dynamics study of spontaneous vesicle formation of amphiphilic molecules. *J. Chem. Phys.*, 116(13):5842–5849, 2002.
- [50] R. Groot. Electrostatic interactions in dissipative particle dynamics - simulation of polyelectrolytes and anionic surfactants. *J. Chem. Phys.*, 118(24):11265–11277, 2003.
- [51] R. Vliet, M. Dreischor, H. Hoefsloot, and P. Iedema. Dynamics of liquid-liquid demixing: mesoscopic simulations of polymer solutions. *Fluid Phase Equilibria*, 201:67–78, 2002.
- [52] R. Vliet, H. Hoefsloot, and P. Iedema. Mesoscopic simulation of polymer-solvent phase separation: linear chain behavior and branching effects. *Polymer*, 44:1757–1763, 2003.
- [53] Y. Kong, C. Manke, W. Madden, and A. Schlijper. Effect of solvent quality on the conformation and relaxation of polymers via dissipative particle dynamics. *J. Chem. Phys.*, 107(2):592–601, 1997.
- [54] R. Groot, T. Madden, and D. Tildesley. On the role of hydrodynamic interactions in block copolymer microphase separation. *J. Chem. Phys.*, 110(19):9739–9749, 1999.
- [55] N. Spenley. Scaling laws for polymers in dissipative particle dynamics. *Europhys. Lett.*, 49(4):534–540, 2000.
- [56] K. Chang and C. Manke. Simulation of polymer solutions by dissipative particle dynamics. *Molecular Simulation*, 25:157–166, 2000.
- [57] P. Español and P. Warren. *Europhys. Lett.*, 30:191, 1995.
- [58] R. Groot and P. Warren. Dissipative particle dynamics: Bridging the gap between atomistic and mesoscopic simulation. *J. Chem. Phys.*, 107(11):4423–4435, 1997.
- [59] M.P. Allen and D.J. Tildesley. *Computer simulation of liquids*. Clarendon, Oxford, 1987.

- [60] L. Harnau and P. Reineker. Equilibrium and dynamical properties of semiflexible chain molecules with confined transverse fluctuations. *Phys. Rev. E*, 60(4):4671–4676, 1999.
- [61] T. McLeish. Tube theory of entangled polymer dynamics. *Adv. Phys.*, 51(6):1379–1527, 2002.
- [62] F.J. Ziemann. *Untersuchungen der lokalen viscoelastischen Eigenschaften von Zellen und Zellmodellen mit einem Magnetkugelmikrorheometer*. PhD thesis, Technical University of Munich, 1997.
- [63] D. Bicout and T. Burkhardt. Simulation of a semiflexible polymer in a narrow cylindrical pore. *J. Phys. A*, 34:5745, 2001.
- [64] T. Burkhardt. Free energy of a semiflexible polymer in a tube and statistics of a randomly-accelerated particle. *J. Phys. A*, 30:L167, 1997.
- [65] M. Dijkstra, D. Frenkel, and H. Lekkerkerker. Confinement free energy of semiflexible polymers. *Physica A*, 193:374, 1993.
- [66] W. Helfrich and W. Harbich. *Chem. Scr.*, 25:32, 1985.

# Acknowledgements

I would like to thank many people without whom this work could not have been done. I am very much grateful to

- ... Dr. habil. Alexei Boulbitch for the introduction to the field of biophysics and patient supervising of my work
- ... Prof. Erich Sackmann for giving me a great opportunity of making a PhD in E22
- ... Prof. Vladimir Sakhnenko for encouraging support over many years
- ... Prof. David Pink and Bonnie Quinn for introducing me to the DPD method and for their hospitality during my stay at the St. Francis Xavier University, Antigonish, Canada
- ... Jörg Uhde for his inspiring experiments
- ... Adam MacDonald for the great 3D visualisations of my simulations
- ... my friends in Munich who made my staying there a wonderful time. These are Alex, Christian, Kheya, Gjertrud, Laurent, Laurent, Guy, Samuel, Felix, Ana, Manfred, as well as the members of the 'russian community' Dassia, Maxim, Kostja, Elena, Nadja, and many others. I am grateful to the Verein Gorod and its KSP Abteilung.
- ... the rest of E22 for the great atmosphere and valuable help